August 2014

Neutron Spectroscopy with Scintillation Detectors using Wavelets

Jessica Hartman
University of Nevada, Las Vegas, Hartma43@unlv.nevada.edu

Repository Citation

Hartman, Jessica, "Neutron Spectroscopy with Scintillation Detectors using Wavelets" (2014). *UNLV Theses, Dissertations, Professional Papers, and Capstones*. 2480.
https://digitalscholarship.unlv.edu/thesesdissertations/2480

NEUTRON SPECTROSCOPY WITH SCINTILLATION DETECTORS USING WAVELETS

By

Jessica Hartman

Bachelor of Science in Mechanical Engineering
University of Nevada, Las Vegas
2012

A thesis submitted in partial fulfillment
of the requirements for the
Master of Science - Materials and Nuclear Engineering

Department of Mechanical Engineering
Howard R. Hughes College of Engineering
The Graduate College

University of Nevada, Las Vegas
December 2014

UNLV | GRADUATE COLLEGE

We recommend the thesis prepared under our supervision by

Jessica Hartman

entitled

Neutron Spectroscopy with Scintillation Detectors Using Wavelets

is approved in partial fulfillment of the requirements for the degree of

Master of Science - Materials and Nuclear Engineering
Department of Mechanical Engineering

Alexander Barzilov, Ph.D., Committee Chair

William Culbreth, Ph.D., Committee Member

Yitung Chen, Ph.D., Committee Member

Gary Cerefice, Ph.D., Graduate College Representative

Kathryn Hausbeck Korgan, Ph.D., Interim Dean of the Graduate College

December 2014

ABSTRACT

NEUTRON SPECTROSCOPY WITH SCINTILLATION DETECTORS USING WAVELETS

by

Jessica Hartman

Dr. Alexander Barzilov, Examination Committee Chair

Associate Professor of Mechanical Engineering

University of Nevada, Las Vegas

The purpose of this research was to study neutron spectroscopy using the EJ-299-33A plastic scintillator. This scintillator material provided a novel means of detection for fast neutrons, without the disadvantages of traditional liquid scintillation materials. EJ-299-33A provided a more durable option to these materials, making it less likely to be damaged during handling. Unlike liquid scintillators, this plastic scintillator was manufactured from a non-toxic material, making it safer to use, as well as easier to design detectors. The material was also manufactured with inherent pulse shape discrimination abilities, making it suitable for use in neutron detection.

The neutron spectral unfolding technique was developed in two stages. Initial detector response function modeling was carried out through the use of the MCNPX Monte Carlo code. The response functions were developed for a monoenergetic neutron flux. Wavelets were then applied to smooth the response function. The spectral unfolding technique was applied through polynomial fitting and optimization techniques in MATLAB.

Verification of the unfolding technique was carried out through the use of experimentally determined response functions. These were measured on the neutron source based on the Van de Graff accelerator at the University of Kentucky. This machine provided a range of monoenergetic neutron beams between 0.1 MeV and 24 MeV, making it possible to measure the set of response functions of the EJ-299-33A plastic scintillator detector to neutrons of specific energies. The response of a plutonium-beryllium (PuBe) source was measured using the source available at the University of Nevada, Las Vegas. The neutron spectrum reconstruction was carried out using the experimentally measured response functions. Experimental data was collected in the list mode of the waveform digitizer. Post processing of this data focused on the pulse shape discrimination analysis of the recorded response functions to remove the effects of photons and allow for source characterization based solely on the neutron response. The unfolding technique was performed through polynomial fitting and optimization techniques in MATLAB, and provided an energy spectrum for the PuBe source.

ACKNOWLEDGEMENTS

This thesis would not have happened without the direction and advice of my advisor, Dr. Alexander Barzilov. Since deciding to join the nuclear engineering program at UNLV, he has been an incredible source of help and encouragement, and it has been a privilege to have him as my advisor and committee chair.

Dr. William Culbreth, Dr. Yitung Chen, and Dr. Gary Cerefice have also provided invaluable knowledge both as instructors and as members of my defense committee. I've already learned much from them and look forward continuing to learn from them in the future.

Dr. Steven Yates and Dr. Erin Peters have also provided crucial support for the completion of this research. Dr. Yates made the University of Kentucky Accelerator Laboratory's accelerator facility available for use. Dr. Peters was willing to assist in running and tuning the accelerator despite the long hours.

I also need to acknowledge the UNLV Graduate and Professional Student Association for providing travel funding to both present this work, and to collect data. In particular, I would like to thank Rebecca Boulton, who was always willing to answer questions and offer advice during the application process.

I would also like thank the UNLV College of Engineering's technical writer, Julie Longo and our administrative assistants, Joan Conway and Jim Boyer. Julie was always willing to provide answers and advice with formatting questions. Joan and Jim were always able to set me straight on which forms needed to be filled out and who I needed to contact, making this process very effective.

DEDICATION

For my parents and sister.

Without your support this would not have been possible.

TABLE OF CONTENTS

LIST OF TABLES

LIST OF FIGURES

CHAPTER 1 - INTRODUCTION

1.1 Project Motivation and Objectives

Accurate assessment of amount of fissile isotopes and special nuclear materials (SNM) in all stages of fuel cycle is crucial in order to enhance safety and security of nuclear facilities and to achieve the nonproliferation goals. While the regulations providing for the SNM acquisition and use are strict, it is possible for SNM to be misplaced, mislabeled, lost or stolen. In certain instances, the nuclear material can be intentionally mislabeled and packaged to avoid scrutiny. Additionally, the material may have been manufactured during a period when the standards and regulations for handling SNM and radioactive sources were not a subject to today's stringent regulations.

Nuclear materials can be assessed by the measurement of ionizing radiation including emissions from spontaneous fission events and induced fission reactions: prompt and delayed neutrons and gamma rays. Furthermore, isotopic neutron sources are widely employed in research and industry. In the case of "orphan" sources, the material has likely been forgotten or abandoned by the party responsible for its use and maintenance. This is especially relevant in industrial applications, where sealed sources are frequently used in the portable equipment. The result is that an orphan source remains undisturbed until it is re-discovered by an uninformed individual. Since the source appears to be a metallic part it can be scavenged and sold as scrap to a recycling facility. The potential of radiation exposure to the public and the environment is serious in such case. Several cases have already been documented where orphan sources have been responsible for the contamination of recycling facilities, as occurred in Algeciras, Spain [1] and most notably, even an entire city, as happened in Goiânia, Brazil [2,3]. While these two incidents involved the loss of photon sources, the loss of neutron sources is also a particular concern in the logging and oil industries. There have been numerous incidents where neutron sources were lost during oil and gas exploration. Between 1956 and 2001, multiple ^{241}AmBe sources were lost during exploration activities, accounting for 74-TBq of radioactivity [4]. One notable incident involved the loss of a 15-curie AmBe source during well logging operations near Pecos, Texas. Reported as lost on September 11, 2012, search efforts failed to find the missing source. It was eventually recovered almost a month later by a member of the general public, 8 miles from the location of the well logging activity [5].

While these incidents stemmed from the ignorance of those who found the sources, there is also a very real possibility that they will be found by people with malevolent intent. According to the IAEA, 2,477 incidents involving orphan sources were reported between 1993 and 2013, with 664 of the incidents being classified as theft or loss, and 424 reported as involved in illicit activities [6]. The use of detectors to examine and classify sources and nuclear materials becomes critical in identifying and stopping potential proliferation of SNM. After the September 11th attacks on the United States, this concern became pressing. Additional detection and monitoring safeguards were implemented to deal with the potential transport of illicit radioactive materials across national borders.

Gaseous ^{3}He detectors were established as the gold standard in radiation detection due to their ability to distinguish between neutron and photon sources [7]. The recent efforts in increasing national security have led to inflation of the demand for ^{3}He detectors. Currently, the methods to measure the neutron emission from fission events rely mainly on thermal neutron detectors equipped with a moderator. The stockpiles of ^{3}He are being constantly depleted, leading to shortages and higher prices. It has also led to increased pressure to develop advanced detection technologies capable of providing comparable quality and efficiency in function [8-10].

Since the fission spectrum contains mainly fast neutrons, detection technologies using fast neutron measurements are relevant for the assay of SNM. The neutron energy data allows characterization of nuclear materials and neutron sources. It can also be applied in remote sensing and source search tasks. Moreover, measurements of spectral distribution of fast neutron flux are important in monitoring of accelerator-based neutron sources and in dosimetry applications.

The objective of this research project was to develop a fast neutron detector with a spectroscopy option. The rigid, low-power detector based on the solid state scintillator EJ-299-33A was studied for fast neutron spectroscopy and identification of neutron sources based on the unique radiation signatures they produce.

1.2 Radiation Detection

Since the discovery of X-rays in 1895 and subsequent development of the spinthariscope in 1903, radiation detection has been a continuously evolving field [11]. Early detectors focused primarily on the application of gas ionization and scintillation detection. Ionization chambers, proportional counters, and Geiger-Mueller counters were designed to take advantage of the ionization and excitation of gas molecules. They focused on the effects caused by a charged particle passing through a gas, producing an electric signal which was directly correlated to ion pair formation [12]. The simplicity of these detectors and the limited information they were capable of providing made them useful primarily as warning systems. They could provide the user with an indication of radiation levels at a given location and offer limited directionality, reporting higher radiation levels near the source but were usually incapable of identifying the type of radioactive material responsible for the reading.

To obtain more detailed information about radiation sources, scintillation detection technology was employed. It relies on the scintillation process to provide critical data used in detection and spectroscopy methods. During the scintillation process, particles from a source pass through the detector medium. They interact with the atoms present in the detector material. When this occurs, scintillation light is produced and collected by the detector. The number of scintillation photons is proportional to the energy of radiation absorbed by the scintillator. The collection process continues for the duration of the measurement, and can be used to develop an energy spectrum for the source [12]. The development of the photomultiplier tube (PMT) triggered subsequent burst of innovations in scintillator development in the 1950s [13]. The majority of modern organic scintillation detectors are crystalline, liquid, and plastic [12,14]. These scintillator materials are manufactured with large hydrogen content, making fast neutron detection possible through proton recoil processes.

1.3 Scintillators

Scintillators can be divided into two main categories - inorganic and organic [12]. Inorganic scintillators tend to exhibit greater light output and linearity than their organic counterparts, but suffer due to an extremely slow response time. Organic scintillators show a reduced light output, but exhibit a quicker response time than inorganic scintillators. These differences typically result in scintillator material being selected based on application. The higher density and greater *Z*-values of inorganic scintillator materials make them ideal for use in gamma-ray spectroscopy applications. The considerable hydrogen content present in organic scintillator material leads to their preferred use for fast neutron detection [12,14]. Of the crystalline scintillator materials that have been developed, only anthracene and stilbene have displayed properties making them acceptable for scintillation applications. Anthracene has the longest history of use and provides the best scintillation efficiency when compared with any other organic scintillator, but it is incapable of providing reliable pulse shape discrimination (PSD) properties. As a result of this, stilbene is preferred for PSD applications, such as discrimination between incident neutrons and photons. It is known to suffer a lower light yield than anthracene, but the ability to carry out PSD makes it useful in situations where anthracene is incapable of providing adequate results [12,14]. The use of these crystalline scintillators was explored extensively during the 1970s, but the fabrication techniques of the time period were ineffective. Machining of the material proved difficult, and crystals could not be easily produced in sizes large enough to be suitable for detector use [15]. The issues surrounding the acquisition of large crystals continue to persist despite recent advances in growing methods, making crystalline scintillators an unpopular material.

Liquid organic scintillators (see Fig. 1) are the most widely used in detectors. Current technology relies mainly on the use of liquid scintillators with PSD to provide accurate identification and verification of materials [16]. This class of scintillators is composed solely of the desired organic material dissolved in an appropriate solvent. Depending on intended application, a wavelength shifter can also be added during the fabrication process. These wavelength shifters are used to tailor the emission spectrum of the detector to be more compatible with that of the PMT which is used with it [12,13].

Figure 1: Liquid Scintillator.

Liquid organic scintillators are fragile and expensive [17]. This is due in part to the liquid nature of the material, and detector casing. Liquid scintillators are typically manufactured with a design as shown in Fig. 2. The aluminum housing is machined and filled with liquid scintillator material and an inert gas bubble, then sealed with a glass disc. While the aluminum housings are not necessarily susceptible to damage, the glass disc secured at the open end of the housing is not as durable. For the example shown, the 6.3-mm PYREX window is subject to cracking or breaking if dropped.

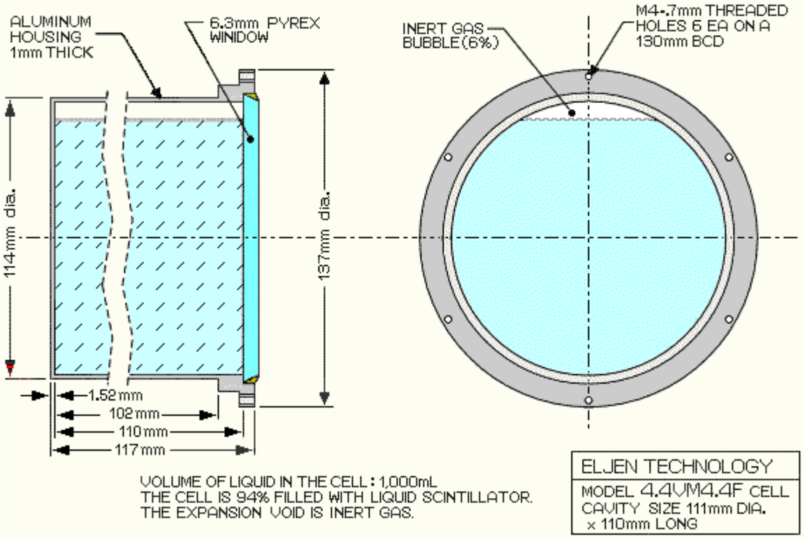

Figure 2: ELJEN Technology Liquid Scintillator Schematic.

Even a simple accident can result in irreparable damage being done to the scintillator, rendering it useless. There is also a known issue with consistency among these detectors, stemming from the impact of solvent impurities. Pulse height differences have been reported as high as a factor of two between samples of the same liquid scintillator due to the unique presence of impurities within each sample [13]. Additionally, there are concerns regarding the toxicity and flammability of liquid scintillators. The liquid scintillator EJ-309, produced by ELJEN Technologies, is chemically toxic, with a flash point of only 77°C, requiring it to be classified as a flammable liquid [18].

The main difference between plastic and liquid scintillators is the state of the scintillator material being used. Plastic scintillators are manufactured in a manner similar to their liquid counter parts. Instead of a liquid solvent, the preferred organic scintillator material is mixed with a plastic solvent during the fabrication process. This difference provides several distinct advantages, such as flexibility and durability, when compared with other commercially available scintillators. The plastic state lends itself to flexibility in design and production, making it possible to fabricate pieces to specified dimensions and shapes.

As can be seen in Fig. 3, it is possible to manufacture plastic scintillator material in a variety of sizes of rods, cylinders and flat sheets. Small diameter fibers have also been developed with various cross-sectional shapes.

Figure 3: Plastic Scintillator Samples.

The relatively low cost of the material also adds credibility to its use as an economical choice for applications where large volume scintillators are required (i.e. for interrogating cargo containers in shipping ports, or trucks at border crosses). These plastic scintillators are also more durable than liquid scintillators by virtue of their state. They do not require a customized casing in order to prevent loss or degradation of material. Due to their solid plastic state, the consequences of dropping this scintillator material are also not as severe as those involved in mishandling a liquid scintillator. Unlike their liquid counterparts, plastic scintillators are also non-toxic and inflammable.

1.3 Spectrum Unfolding

In nuclear measurements, it is often necessary to extract the spectral distribution from data output by the detector. In its raw form, this data is not the energy spectrum of the material being examined; it is rather a sum of all the detector responses for particles of different energies. Typically, measurements are recorded through the use of time or event cutoffs, where an event correlates to a single particle entering the scintillation material and generating a light output. Using an event cutoff can be preferable as it requires a certain number of events to occur before the measurement ends. It ensures that there is a large enough data set to allow for statistical comparison and reduction of possible fluctuations. In either case, the resulting energy distribution recorded by the detector is the summation of the scintillation light responses to all particles of different energies emitted by the source.

In order to reconstruct the incident particle energy spectrum for a given source, spectrum unfolding techniques are applied to the energy distributions recorded by a detector. The use of monoenergetic response functions provides a basis for the unfolding process of energy spectrum. These functions can be developed from calculated responses or evaluated excitation data, but require validation with experimental measurements [19]. The response functions are typically used in the form of matrices of data, as a function of several variables including the incident neutron energy, and angle of incidence.

In the case of scintillation materials with PSD capabilities, such as EJ-299-33A, it is possible to produce separate spectra from the neutrons and photons. An example of the difference between the spectra produced with and without PSD is shown in Fig. 4. This particular example is developed from the pulse height measurements of a DT neutron generator, collected with a NE213 detector [20].

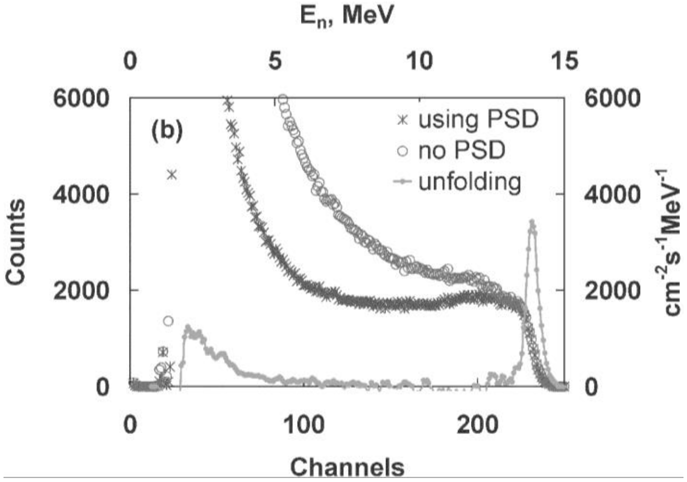

Figure 4: Pulse height spectrum of a DT neutron, produced by an NE213 detector, using spectrum unfolding [20].

The recorded pulse height distributions for a 14-MeV neutron source are shown with and without PSD applied. The neutron spectral distribution reconstructed using the neutron-only data after the PSD with an unfolding computer code is also shown.

The spectrum unfolding techniques range from simple to complicated and memory intensive, requiring additional parts or components to be added to the detector system, or even post-processing to be performed at a computer station [21].

In order to extract the incident spectral data from a measured energy distribution, it is necessary to know the monoenergetic response functions of the scintillator material used.

Since these functions are entirely dependent on the chemical composition of the scintillator material, they must be determined experimentally, or through the use of computer codes such as MCNP or GEANT. To facilitate the spectral unfolding process, it is preferable to use response functions for a range of monoenergetic neutron sources with a consistent energy step. Selection of the energy step is primarily an optimization problem. A smaller energy gap will produce more accurate results of the unfolding process, but it can become memory intensive to store the extra functions required, without significantly improving the unfolded results.

The response functions of scintillators can be complex. Among the factors leading to it are the light yield as a function of particle energy, the edge effect, detector resolution, and the scattering caused by the hydrogen and carbon used in scintillator materials [12].

While there is a variety in the spectra unfolding techniques currently used [21-24], they all assume the application of the Fredholm integral (Eqn. 1).

$$N_i = \int R_i\left(E\right) S_j\left(E\right) dE \tag{1}$$

This assumption provides a linear formula which is ideally suited to the purpose of spectral unfolding by relating the pulse height spectrum as measured by a scintillation detector and the differential energy spectrum. In the integral, N_i represents the counts for a given channel i in the pulse height spectrum, $R_i(E)$ represents the response function of channel i to particles with energy E, and $S_i(E)$ is the differential energy spectrum which would be used to identify the source material [12]. While the integral form is useful, it is preferable to consider a different form of the integral. This form can be equated to the use of a multichannel analyzer, which allows the integral to be reduced to the following discrete summation:

$$N_i + e_i = \sum_j R_{ij} S_j \tag{2}$$

where N is the count for a given channel i, R is the relevant response for the given channel and a given energy bin j, and S becomes a coefficient indicating the presence of a source element, and e_i represents any effects which might be indescribable using a given model [12]. In performing the spectral unfolding, N is the energy distribution as measured by the detector. It is reconstructed as the summation of the unique response functions R corresponding to different particle energies, with S acting as a variable which must be determined in order to properly unfold the initial data (N) into its component functions (R). The mathematical approaches are applied to the detector response functions and implemented as computer codes [12,20].

1.4 Wavelets

In the engineering and mathematics fields, application of Fourier Transforms has become a standard method of signal analysis [25,26]. The Fourier Transform can be labeled as a special case of a continuous wavelet transform where the mother wavelet $\left(\psi(t)\right)$ is defined such that:

$$\psi(t) = e^{-2\pi i t} \tag{3}$$

Although the potential of wavelets is still largely overlooked, their use in applications has been gaining increasing popularity in both the academic and research communities in recent years [27-29]. Research has also demonstrated that wavelets provide superior results in performing signal analysis functions when compared with the use of the Fourier Transform [26]. The concept of the wavelet is also applicable in the nuclear field. They have been considered for multiple nuclear applications, such as solving neutron transport equations [30], neutron diffusion problems [31,32], and pulse shape discrimination [33]. Research into their application for digital pulse processing has also been carried out [34,35], but focused primarily on the development of filtering techniques for raw signals.

While the principle wavelet application has traditionally been signal analysis, the inherent properties of this function makes it worthy for use in spectra unfolding techniques. By treating the detector response of a source as a signal, it is possible to fit the general wavelet equation (Eqn. 4) to this function and store it as an equation rather than a matrix of values. This can potentially reduce the onboard memory required in order to properly store and perform necessary the necessary operations for spectral unfolding. In addition, wavelet treatment of responses allows smoothing of noisy data, which is typical for nuclear measurements.

The continuous form of Eqn. 4 was adapted to model and store the detector response functions as wavelets (Ψ_n). This was done by assuming $R(E)$ to be the characteristic, monoenergetic response functions measured by a given detector with respect to the source energy (E). The only variables which needed to be defined were the scale (a) and shift (b) applied to the response function. Scale can be defined as the time frequency of the wavelet and will dilate the spectrum, while shift focuses on translating the spectrum.

$$\Psi_n = \int_{-\infty}^{\infty} R(E) \frac{1}{\sqrt{a}} \varphi\left(\frac{E-a}{b}\right) dE \tag{4}$$

Applying wavelets to the raw responses incorporates the smoothing function inherent in the use of any wavelet equation. Each wavelet is equivalent to the application of a high pass filter and low pass filter to a signal. This effectively deconstructs the response into two components, which are referred to as approximations and details. Approximations are similar to the de-noised signal created by applying a low pass filter to a signal, and are synonymous with the smoothed response function. The details result from the application of a high pass filter, in this case to the response function, and are considered "noise" which is removed from the response function and discarded [36].

CHAPTER 2 – LITERATURE REVIEW

2.1 Background

Computer codes for spectral unfolding such as FORIST [37], MAXED [38], GAVEL [39] and others have been developed. Despite this, spectral unfolding remains a relevant concern in identifying radioactive materials. Most of these techniques rely on the use of one of the following methods: regularization, least-squares regression, maximum entropy, iterative methods, and stochastic techniques.

2.1 Regularization Methods

The goal of regularization methods is to find an acceptable approximate solution which will minimize the error of the fit. In regularization, this minimization is achieved through the inclusion of a penalty. For the purposes of spectral unfolding, this penalty could be applied as a smoothness constraint. The use of this constraint would ensure that, of the spectra solution pool considered, and spectrum solution showing extreme or considerable oscillating behavior would be excluded from further consideration [21].

Chi-squared is typically used as the standard measure of fit for mathematical unfolding techniques, with the basic form of:

$$\chi^2 = \left(N - RS\right)^T C_N^{-1} \left(N - RS\right) \tag{5}$$

where *N* is the measured spectrum, *R* is the solution spectrum, and *S* is the components of the fluence vector. C_N is the inverse of the measurements covariance matrix, typically defined as the diagonal matrix: $C_N^{-1} = diag\left(\frac{1}{\sigma_1^2}, \frac{1}{\sigma_2^2}, \ldots, \frac{1}{\sigma_n^2}\right)$. The problem is then defined through the use of the following Lagrange polynomial, where λ is the regularization parameter and the function *H* becomes the stabilizer [40].

$$L = (N - RS)^T C_N^{-1} (N - RS) + \lambda H(S) \tag{6}$$

2.1.1 Linear Regularization

Linear regularization makes use of a specific family of stabilizer functions. Defined below, this family is dependent on the k^{th} derivative of the solution spectrum [21]:

$$H^{(k)} = \int \left(\frac{d^{(k)} s}{dE^k} \right)^2 dE \tag{7}$$

By considering the discrete case of this function, it is possible to rewrite Eqn. 4 as:

$$L = (N - RS)^T C_N^{-1} (N - RS) + \lambda S^T H^{(k)} S \tag{8}$$

By selecting a suitable solution spectrum for *H*, the resulting minimization of *L* will lead to the following relationship:

$$S = \left(R^T R + \lambda H^{(k)}\right)^{-1} R^T N \tag{9}$$

While linear regularization is similar to a simple, direct inversion of the *R*-matrix, the *λH^((k))* term is included prior to carrying out a matrix inversion. Adding this term will typically solve the problems associated with performing a direct matrix inversion, making it possible for a physically relevant spectral solution to be determined [21].

2.1.2 Non-linear Regularization

While it is possible to select stabilizer functions which will lead to linear equations, functions can also be selected to produce non-linear equations. One example of this uses Fisher information. It has been demonstrated that this method is capable of minimizing the difference between calculated and measured activation rates for neutron energy distributions when used in conjunction with a constraint to minimize the Fisher information [41]. In order to obtain the Fisher information, the following relation is used, where E is the energy, and Φ_t indicates the true spectral solution:

$$I(\Phi) = \int \frac{1}{\Phi}\left(\frac{d\Phi}{dE}\right)^2 dE \tag{10}$$

From this relation it is possible to see that the Fisher information (I) provides an estimation of the error between the actual and calculated spectra solutions. As the mean squared error (ϵ2) between the two solutions increases, I will decrease as indicated by the following Cramer-Rao inequality, where $\varepsilon^2 = [\Phi - \Phi_t]^2$:

$$\varepsilon^2 I(\Phi) \geq 1 \tag{11}$$

When no information about the true solution exists, then the estimation error will increase and the Fisher information term will reach a minimum. Unlike other regularization methods, the ratio of the squared derivative ratio to the flux (Eqn. 8) ensures that use of the Fisher information term till produce a smooth solution without losing unique features of the spectra, such as discontinuities [41].

2.2 Least Squares Methods

Developed in the early 1800s, the least squares method (LSM) has become a standard approach in data fitting problems. This spectrum unfolding technique has been proven reliable in data fitting applications and applies a best fit approach in order to develop the energy spectrum of a source from a given detector response function. This is achieved by finding a spectral solution which will minimize the over-all value of the chi-squared term. In applying the LSM to neutron spectral unfolding, chi-squared represents the sum of the differences between the observed (recorded) values of the response function and their respective fitted values as taken from a defined spectrum solution.

2.2.1 Non-linear Least Squares

In focusing on a least-squares approach with the inclusion of a chi-squared term, it is possible to use either the standard expression (Eqn. 3) or a more general form. The simplest approach is of course to use the standard chi-squared expression. Unfortunately when $R^T C_N^{-1} R$ is non-singular, the minimization of chi-squared will result in a solution identical to that found by performing a direct inversion of the *R*-matrix. This will also result in the solution suffering the same problems caused by a direct inversion such as increased “noise” levels in the resulting spectrum, and a lack of physical meaning due to significant oscillations and negative fluence values [21].

In order to avoid these difficulties, it can be preferable to assume a less specialized form of the chi-squared expression, such as:

$$\chi^2 = \left(N - R(r)S\right)^T C_N^{-1}\left(N - R(r)S\right) + \left(S_0 - S\right)^T C_S^{-1}\left(S_0 - S\right) + \left(r_0 - r\right)^T C_R^{-1}\left(r_0 - r\right) \qquad (12)$$

For this example, S_0 serves as the initial solution spectrum, C_S and C_R are still covariance matrices, but unlike C_N, they are not generally diagonal in nature. The response functions are indicated by $R(r)$ and considered dependent on the given set of parameters r, with r_0 acting as the initial parameter estimate [21].

Minimization of the chi-squared term is then carried out subject to the additional restriction that the spectrum solution data satisfy the original matrix equation (Eqn. 2). Through the selection of an appropriate solution spectrum (S_0), it is possible to produce a result which is close to a physically reasonable solution. While the use of a non-standard expression for chi-squared is more likely to produce an acceptable solution, the optimization of this problem is non-linear, making it less than ideal [21,42].

2.2.2 Linear Least Squares

To solve the minimization problem associated with the use of a general chi-squared expression, most computer codes will linearize the expression prior to any data manipulation. In order to do this, a Taylor approximation is assumed to replace the constraint derived from Eqn. 2. This leads to the formation of the following expression for the minimization problem:

$$N = N_0 + \left[\left(\left. \frac{dR(r_0)}{dr} \right|_{r=r_0} \right) \otimes (r - r_0) \right] S_0 + R(r_0)(S - S_0) \qquad (13)$$

Due to the complexity of the expression derived from this, linear least squares methods can be difficult to properly apply and use [21]. This method has been implemented frequently through the use of computer codes, and although the derivation is complicated, the method has been proven to work. It serves as the basis for many of the computer codes which have been developed to perform spectra unfolding tasks. This particular method is most effective when both a considerable amount of a piori information and measurement results are available. Unfortunately, it does not provide a solution for the presence of negative fluence values [42].

2.3 Maximum Entropy Method

The maximum entropy method (MEM) is based on the application of the maximum entropy principle. As the name suggests, the goal of this method is to select a spectrum solution to Eqn. 2 which will maximize the relative entropy of *S*. Although it can be defined as a special case of regularization, MEM stands apart from the previously detailed methods because it can be justified through the application of information theory. A formal argument has been published, indicating that MEM is the only generic means of solving the spectrum unfolding problem which does not produce inconsistencies [43]. This method hinges on the use of a priori data, which can consist of recorded or calculated data values, uncertainties, correlations, or any other available information about the experiment [42]. To properly apply the method, a physical constraint must be implemented to compensate for the unknown impact of effects (e_i) such as statistical fluctuations or deviations between R_i (Eqn. 1) and the actual response. This constraint is user defined, and can be defined so as to restrict the spectrum solutions to those which will yield a viable solution that does not exceed the allowed limit for the undefined effects [21].

2.4 Iterative Unfolding Methods

Iterative unfolding methods are almost synonymous with the use of computer codes to unfold neutron spectra. These methods rely on the use of an initial spectrum estimate and unique function based on the measurement properties, uncertainty, response function data, and previous spectrum estimates. The relation between the unfolded spectrum and the initial spectrum is rarely clear, and can be difficult to determine even after performing the iterative procedures [21]. The greatest challenge in applying iterative methods is that they solutions they produce exhibit an extreme sensitivity to the initial guess spectrum provided by the user [42,43]. Iterative procedures have been attempted using the Richardson-Lucy algorithm. While this approach reduces the sensitivity of the spectrum solution to the initial spectrum selected, research indicates that selection criteria are still necessary and must be given proper consideration in order to produce viable results [44].

2.5 Stochastic Methods

Stochastic methods are based on the use of the theory of probability to develop an energy spectrum from an initial detector response function. Inclusion of additional features or parameters may be required to obtain a physically meaningful result. Among the stochastic methods currently in use are the Monte Carlo method, genetic algorithms and neural networks [21]. Although the Monte Carlo method is the oldest, genetic algorithms and neural networks can prove to be more resilient. The Monte Carlo method is a static method, it lacks the ability to “learn” as it processes information. Genetic algorithms and neural networks offer a sharp contrast in this area. Both are based loosely on a biological ability to learn and improve their efficiency or results in the long term.

2.5.1 Monte Carlo Methods

Initially presented by Sanna and O’Brien in 1971, the Monte Carlo method focuses on folding a response function into a randomly selected neutron spectrum to find the count distribution for that particular spectrum. These calculated counts are then compared to a measured distribution to determine if there is an acceptable agreement between the two [45]. In general Monte Carlo methods try to produce a spectrum by averaging a significant number of acceptable spectra. Acceptable spectra are typically selected as being non-negative and providing a relatively good fit for the data in question [21]. This method offers a more traditional approach that has been proven to work, and has been trusted for several decades. Use of the Monte Carlo method is typically accomplished through lengthy and complex computer codes such as the aptly named Monte Carlo Neutron Particle Transport code produced by Los Alamos National Laboratory.

2.5.2 Genetic Algorithms

Originally suggested as a method for spectra unfolding in the 1990s, genetic algorithms are designed to treat problem solutions in a manner similar to biological systems. This allows for the combination and alteration of an initial set of solutions over successive “generations” to eventually produce an ideal solution (spectrum result) [46]. Genetic algorithms are based on “survival of the fittest”, with a solution spectrum being continually refined through successive generations of solutions, each of which incorporates a pair of spectra solutions from the last generation to produce two new solutions which will be used to create the next generation. These algorithms also mimic the biological potential for mutation by randomly altering the spectra being used [47].

The use of genetic algorithms is a multi-step process. First, a large assortment of potential solutions is created as a set of binary strings. From the initial population, a small portion is selected based on a “fitness test.” This test determines which solutions provide the best fit for the true value of the prospective solution, ranking them accordingly. Once ranked, those solutions with the highest rankings are selected and copied, with the rest being discarded from the computation. Pairs of the selected solutions are then selected at random and a portion of one parent spectrum is exchanged for the same portion of its partner to produce two new solution spectra. This cycle of selection, elimination, and combination is then repeated until the solution with the best fit is found [48,49].

2.4.3 Neural Networks

The algorithms used in neural networks are designed to learn and optimize a problem [21]. Each network can be trained to associate input functions with output functions, just as a child would learn to associate a letter of the alphabet with a sound. In the application of spectrum unfolding, it is possible to identify the detector measures as the input, and the expected spectra as the output. These networks are particularly effective when developed as computer codes, and have also been proven to have a high level of performance [50] but they can require intensive programming during the initial learning phase in order to return the proper output function for a given set of data. Unlike genetic algorithms which are based on trying to refine a solution through successive “generations,” neural networks are “taught” to recognize certain spectra models and compare them to the spectrum it sees. Although the calibration may be time consuming, the process itself can be relatively quick as the network learns to accurately identify the incoming data.

CHAPTER 3 - NEUTRON SPECTROSCOPY TECHNIQUE

3.1 Procedure

The primary concern was to develop a technique comparable and ideally preferable to those available at the time. It needed to be easily incorporated into the onboard electronics of a portable detector, without requiring significant increases to the available memory. The technique also needed to function within reasonable time limits while still providing reliable results.

To this end, the research presented here has focused on the development of a spectra unfolding technique for scintillation detectors based on the application of wavelets. The response functions were developed for a plastic scintillator material and subsequently stored as unique wavelets. These responses were then used in conjunction with the theoretical response functions of modeled sources in order to develop an unfolding technique based on fitting the sum of the monoenergetic wavelet-processed response functions to the polyenergetic source response function. The resulting coefficients were then compared with known spectral distributions to determine the validity of the unfolding result.

Experimental validation was also carried out using the neutron energy spectrum obtained from a PuBe source and the monoenergetic response functions measured at the University of Kentucky's Van de Graaff Accelerator Laboratory (UKAL). This facility housed an accelerator capable of producing monoenergetic neutron beams across a range from 0.5 MeV to 24 MeV, with 100-keV steps.

3.2 Response Functions

Since spectra unfolding techniques are based on the use of stored response functions, the most important aspect of developing this project was the development of these functions. Neutron response functions were modeled using version 2.7.0 of the Monte Carlo N-Particle eXtended (MCNPX) code developed by Los Alamos National Laboratory [51]. These response functions were developed for a plastic scintillator EJ-299-33A using the geometry shown in Fig. 5. The model consisted of a single, isotropic, monoenergetic point source positioned 20 cm from the cylindrical body of plastic scintillator material with 2 inch by 2 inch dimensions.

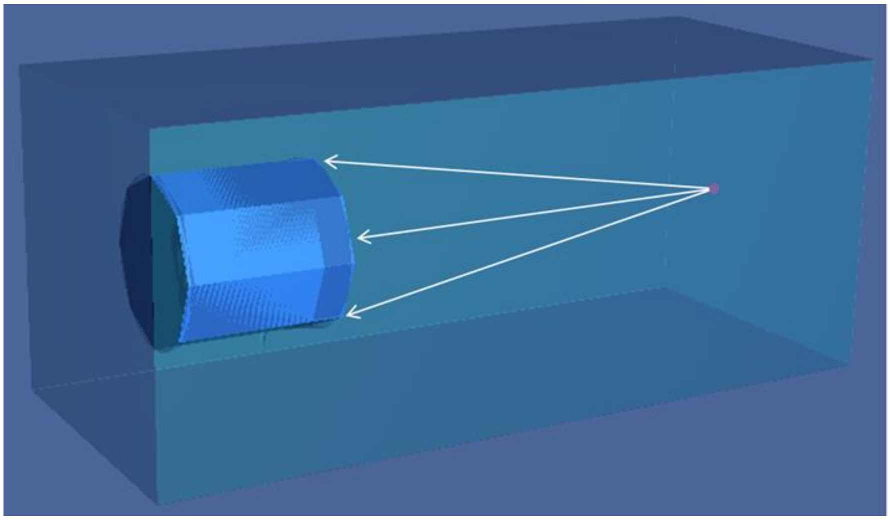

Figure 5: MCNPX geometry for response function modeling.

3.2.1 Scintillator Modeling

The material properties of the plastic scintillator were selected to match those of the novel EJ-299-33A plastic scintillator produced by ELJEN Technology. Despite the selection of this neutron detection medium, the wavelet-based unfolding technique is applicable for use with any desired medium. It will only be necessary to characterize the appropriate material and store the resulting response functions in place of those developed here.

The EJ-299-33A scintillator material was selected for modeling because of its inherent PSD properties [52]. This feature allows for discrimination between the events caused by neutron and gamma-ray interactions, making it possible to isolate neutron counts and focus on the neutron spectrum being generated by a source. Since response functions are dependent on the material type and the scintillator size, it is necessary to model the scintillator cell with the appropriate chemical composition and dimensions. While minor allowances can be made for differences in material fabrication, significant variation in the composition, particularly the hydrogen content, leads to the production of irrelevant and erroneous spectral data. To avoid this, the plastic scintillator material card for the MCNPX input file was defined based on the material specifications (Table 1) provided by ELJEN Technology [53].

Table 1 – Scintillator material specifications for EJ-299-33A.

Properties	
Light Output	56%
Material Density	1.08 g/cc
No. H Atoms per cc	$5.13\text{x}10^{22}$
No. C Atoms per cc	$4.86\text{x}10^{22}$
Scintillation Efficiency	8,600 γ/1 MeV e^-

Since anthracene provides the gold standard for light output among organic scintillators it has traditionally been used as a reference for light output values. As a result, the light output of modern scintillators is often provided as a percentage of anthracene light output [14]. This convention was used for the value reported in Table 1.

A source definition (SDEF) card was used to model the sources in the MCNPX input files. Each source was defined as being an isotropic, monoenergetic, neutron point source as shown below in Fig. 6. In order to define the point source, a spherical macrobody cell was modeled. This "starting" cell was then identified as the location of the source using the position (pos) and cell (cel) identifiers. The particle type and energy were defined using the par and erg identifiers respectively. Using par=n, defined it as a neutron source, and for the given example, erg defined the source energy as a discrete value of 0.2 MeV.

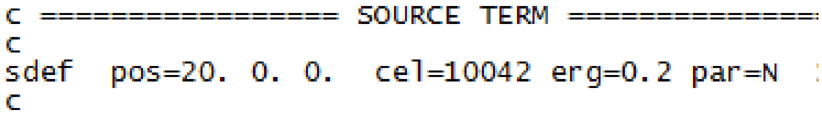

```
c ================== SOURCE TERM ===============
c
sdef  pos=20. 0. 0.  cel=10042 erg=0.2 par=N
c
```

Figure 6: SDEF card used for MCNPX input files.

The same SDEF card arrangement was used to generate each response function for a range of discrete source energies between 0.1 MeV to 14 MeV. Response functions were created with a step size of 0.1 MeV to allow for step size optimization of the unfolding procedure. Developing all of the responses at this resolution made it possible to determine the minimum number of stored functions which could be used in spectral reconstruction. The wavelet-based spectral unfolding technique was implemented using response functions with a 0.1-MeV, 0.2-MeV, 0.5-MeV, and 1.0-MeV step to determine which step size would be the most reasonable for use. The inverse relationship between step size and accuracy of the unfolded spectra makes it necessary to determine a minimum step size which will still produce an appropriate result.

To complete the computational study of this method, it was also necessary to produce a response for a known neutron source. For the purposes of this research, a ^{252}Cf source was modeled using MCNPX. The geometry of the system was identical to that used to generate the response functions, the only changes made were to the SDEF card (Fig. 7).

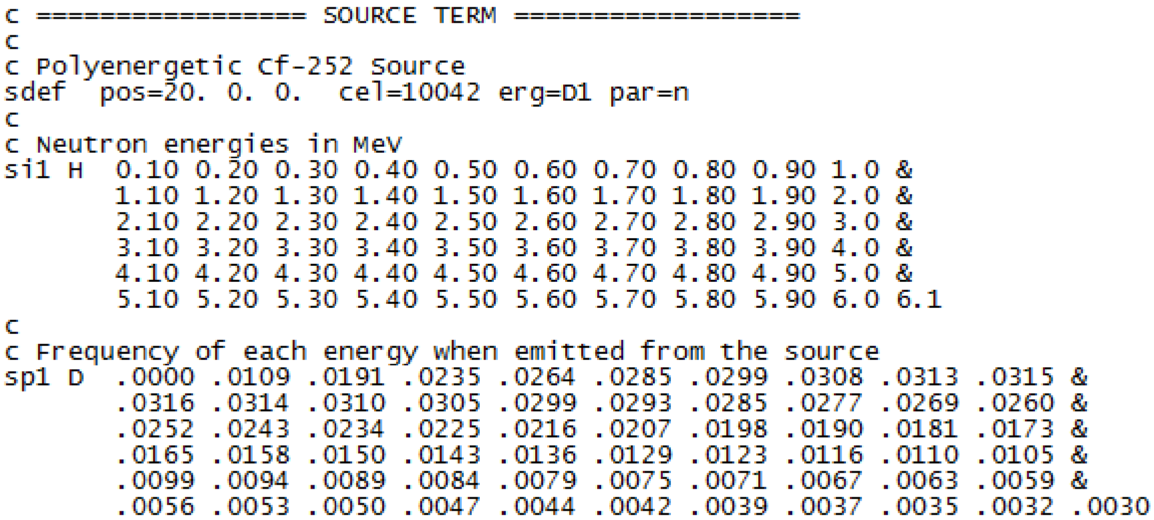

```
c ================== SOURCE TERM ===================
c
c Polyenergetic Cf-252 Source
sdef  pos=20. 0. 0.  cel=10042 erg=D1 par=n
c
c Neutron energies in MeV
si1 H  0.10 0.20 0.30 0.40 0.50 0.60 0.70 0.80 0.90 1.0 &
       1.10 1.20 1.30 1.40 1.50 1.60 1.70 1.80 1.90 2.0 &
       2.10 2.20 2.30 2.40 2.50 2.60 2.70 2.80 2.90 3.0 &
       3.10 3.20 3.30 3.40 3.50 3.60 3.70 3.80 3.90 4.0 &
       4.10 4.20 4.30 4.40 4.50 4.60 4.70 4.80 4.90 5.0 &
       5.10 5.20 5.30 5.40 5.50 5.60 5.70 5.80 5.90 6.0 6.1
c
c Frequency of each energy when emitted from the source
sp1 D  .0000 .0109 .0191 .0235 .0264 .0285 .0299 .0308 .0313 .0315 &
       .0316 .0314 .0310 .0305 .0299 .0293 .0285 .0277 .0269 .0260 &
       .0252 .0243 .0234 .0225 .0216 .0207 .0198 .0190 .0181 .0173 &
       .0165 .0158 .0150 .0143 .0136 .0129 .0123 .0116 .0110 .0105 &
       .0099 .0094 .0089 .0084 .0079 .0075 .0071 .0067 .0063 .0059 &
       .0056 .0053 .0050 .0047 .0044 .0042 .0039 .0037 .0035 .0032 .0030
```

Figure 7: MCNPX source card used to model a ^{252}Cf source with a histogram energy distribution.

Instead of detailing a monoenergetic point source, the entries were changed to create a ^{252}Cf source with a histogram energy distribution between 0.1 MeV and 6.1 MeV, using 0.1-MeV increments. The use of a histogram distribution also required that the frequency of emission for each energy value be included in the input card as well.

Both the monoenergetic response functions and the ^{252}Cf response were generated as pulse height tallies through the use of MCNPX's F8 tally, with the F6 tally applied to convert from units of MeV to MeVee. An example of the tally card for protons is included in Fig. 8. Six F8 tallies were created using the anticoincidence light (PHL) option. Each tally was uniquely assigned to track the responses of protons, alpha particles, deuterons, tritons, or heavy ions (boron and carbon) produced by source neutron interactions. The sixth F8 tally (designated as F58 in the input files) was used to track all responses of all particles produced by source neutron interactions. Since the F8 tally is designed only to output the pulse height data for photons and electrons, it is necessary to include the PHL option in order to determine the pulse height distributions of other relevant particles [51]. An additional F8 tally was included to determine the response function for the summation of all resulting particles, for comparison with the individual particle tallies.

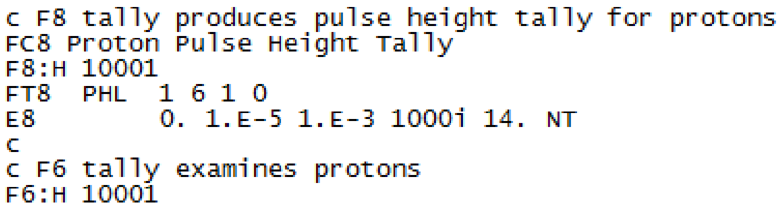

```
c F8 tally produces pulse height tally for protons
FC8 Proton Pulse Height Tally
F8:H 10001
FT8  PHL  1 6 1 0
E8        0. 1.E-5 1.E-3 1000i 14. NT
c
c F6 tally examines protons
F6:H 10001
```

Figure 8: Example MCNPX tally cards for protons produce by source neutrons.

The energy range for the response functions was divided into 1000 energy bins between 0.001 MeV and 14 MeV. A zero bin (0.) and an epsilon bin (1.E-5) were also included for the tallies as suggested in the MCNPX manual. The zero bin was created to store nonanalog knock-on electrons with negative scores. The epsilon bin was included to catch the particle(s) of interest which pass through the designated cell without depositing any energy. In the example given, the epsilon bin was included to collect those protons which lost less than 0.001 MeV in the scintillator cell, effectively separating out those which exited the scintillator without depositing any energy.

3.3 Unfolding Procedure

Several examples of the MCNPX generated response functions are shown in Fig. 9. These response functions display data tallied only in the proton pulse height tally. As previously mentioned, one tally was used to collect the responses of all particles, while others were included to determine the individual responses for unique particles. Comparison of this data was used to verify that the collected response function came primarily from the proton recoil interactions between source neutrons and the scintillator material used. In general, the contribution of the alpha particles, deuterons, and tritons was negligible compared to that of protons. Heavy ions showed some contribution to the response function, primarily between 0.001 MeV and 1.5 MeV for source energies below 4 MeV. Between 4 MeV and 14 MeV, the impact of the heavy ions on the overall response function was reduced and the defining features of each function were determined by the protons. Heavy ions still made a contribution to the modeled response functions, but the proton contribution was far more significant within this energy range.

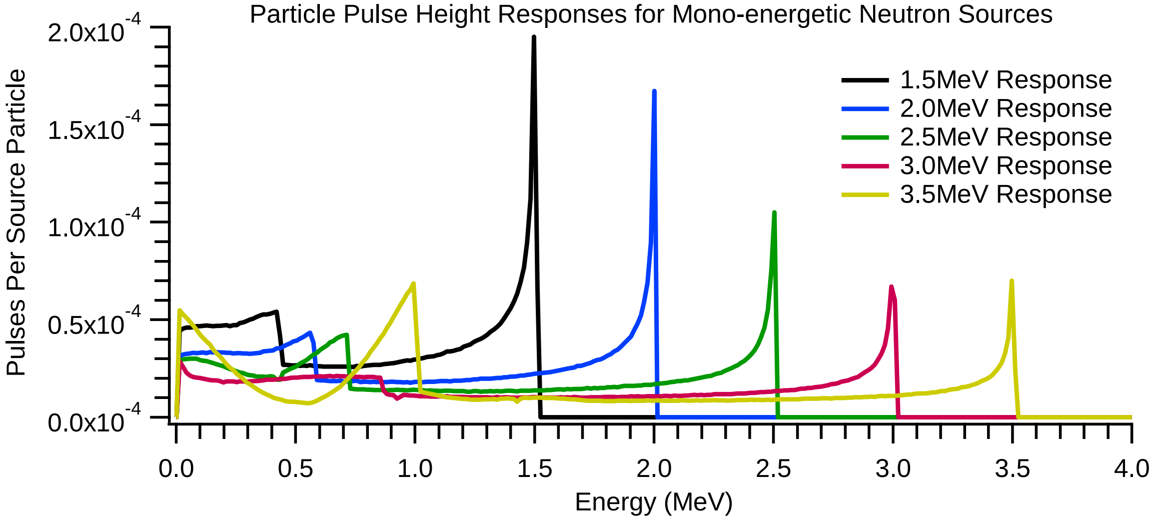

Figure 9: EJ-299-33A response functions for selected monoenergetic source energies.

MCNPX recorded the response functions as two columns of data, each with a thousand points, correlating to the pre-defined energy bins from the tally cards and the particle counts for each energy bin (counts were normalized per single source neutron). Using this information, it was possible to generate each response function as a matrix of static values and import them into MATLAB R2012b [54]. The commands available through MATLAB's Wavelet Toolbox [55] were utilized to fit wavelets to each response function and store them for later use. The result were wavelet models which closely matched the original response functions generated by MCNPX. An example of the similarity between the MCNPX response function and the wavelet function for a 5-MeV source energy is included in Fig. 10. As can be seen from the plot, the wavelet model accurately reproduced the key features of the response function, while also providing a smoothing effect.

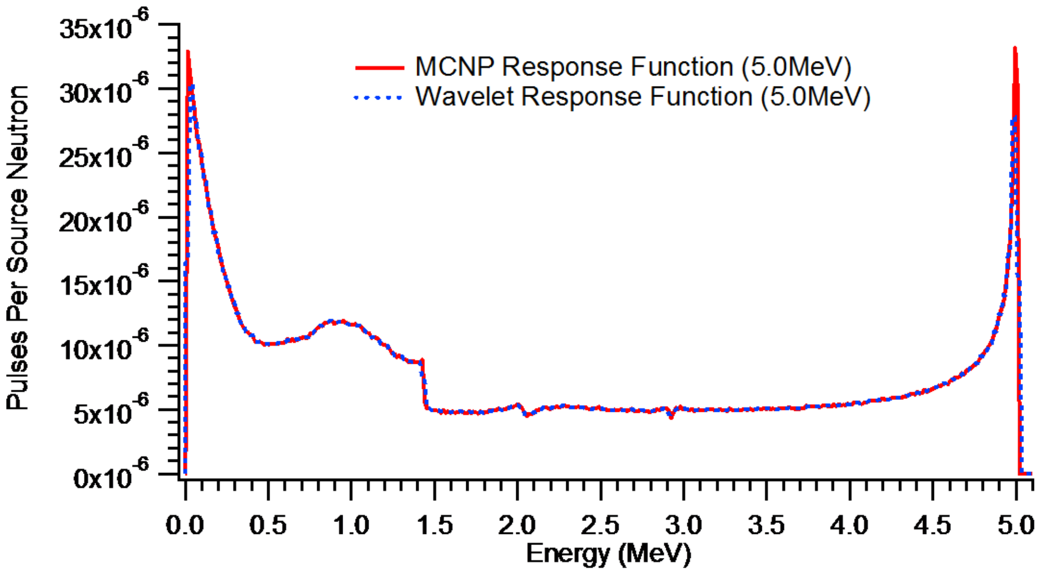

Figure 10: Comparison of the MCNPX generated response function with that of the wavelet smoothed response function for 5.0-MeV.

After creating the wavelet models, the next step was to carry out the spectral unfolding process. MATLAB was utilized to perform the calculations, this time through the optimization of a polynomial fit. The **fmincon** function was selected, and the equation was entered according to the model from Eqn. 2 [56]. Experimentation with the initial values provided for the coefficients revealed that the fitting function performed best when the initial values were entered as a matrix of zeroes. Additional testing also produced the best fitting results when possible coefficient values were limited to a range between 0 and 1.

The fitting process was tested using calculated response functions with incremental steps of 1 MeV and 0.5 MeV. The resulting fits were plotted against the ^{252}Cf response to determine which provided a more reasonable reproduction of the initial source response produced by the EJ-299-33A scintillator cell (Fig. 11). While the results of this step did not provide conclusive proof that the technique was valid for spectral unfolding, they did verify that the reconstruction was producing a fitted response which reasonably recreated the ^{252}Cf response.

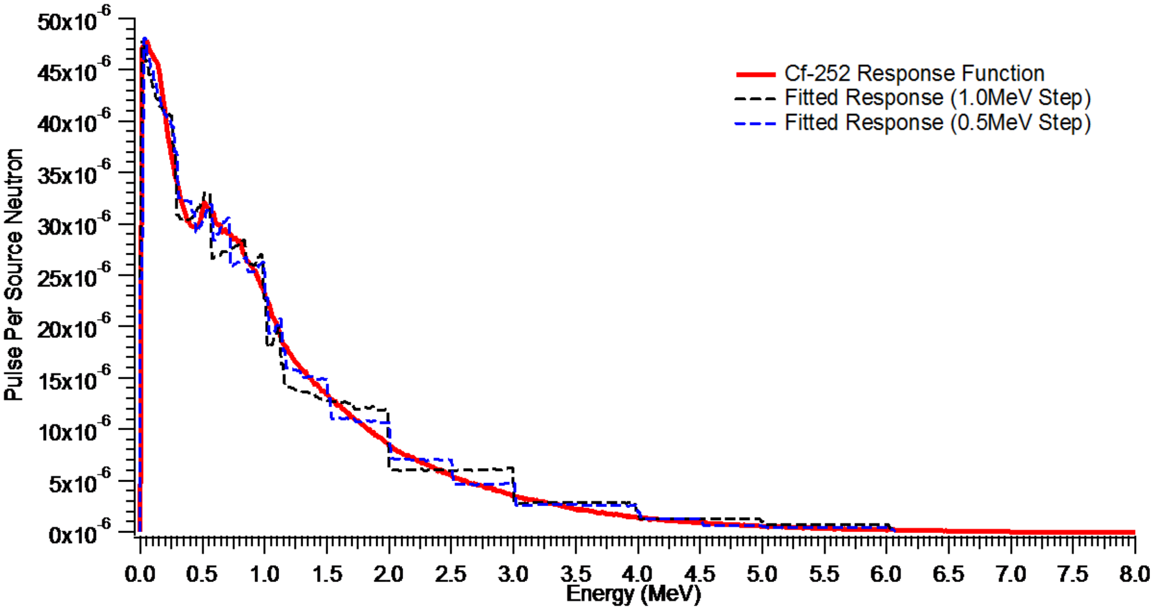

Figure 11: Comparison of the least squares fitting technique using 1.0-MeV and 0.5-MeV steps to fit the summation of response functions to a ^{252}Cf response function.

To test the unfolding method the coefficients generated by this fitting procedure were compared with the theoretical ^{252}Cf energy spectrum developed from the following empirical relation, where *N(E)* is the number of neutrons per energy value (*E*) [57]:

$$N(\mathrm{E}) \propto e^{-(1.036/\mathrm{MeV})E} \sinh[((2.29/\mathrm{MeV})\,\mathrm{E})^{1/2}] \qquad (14)$$

The spectrum produced by this formula is shown in red in Fig. 12. The coefficients produced by fitting the ^{252}Cf response with 0.5-MeV and 1.0-MeV interval response functions are also plotted for comparison. Although the results are not identical, they show enough distinction to indicate that the technique is capable of similar unfolding quality as other currently available techniques [58-60].

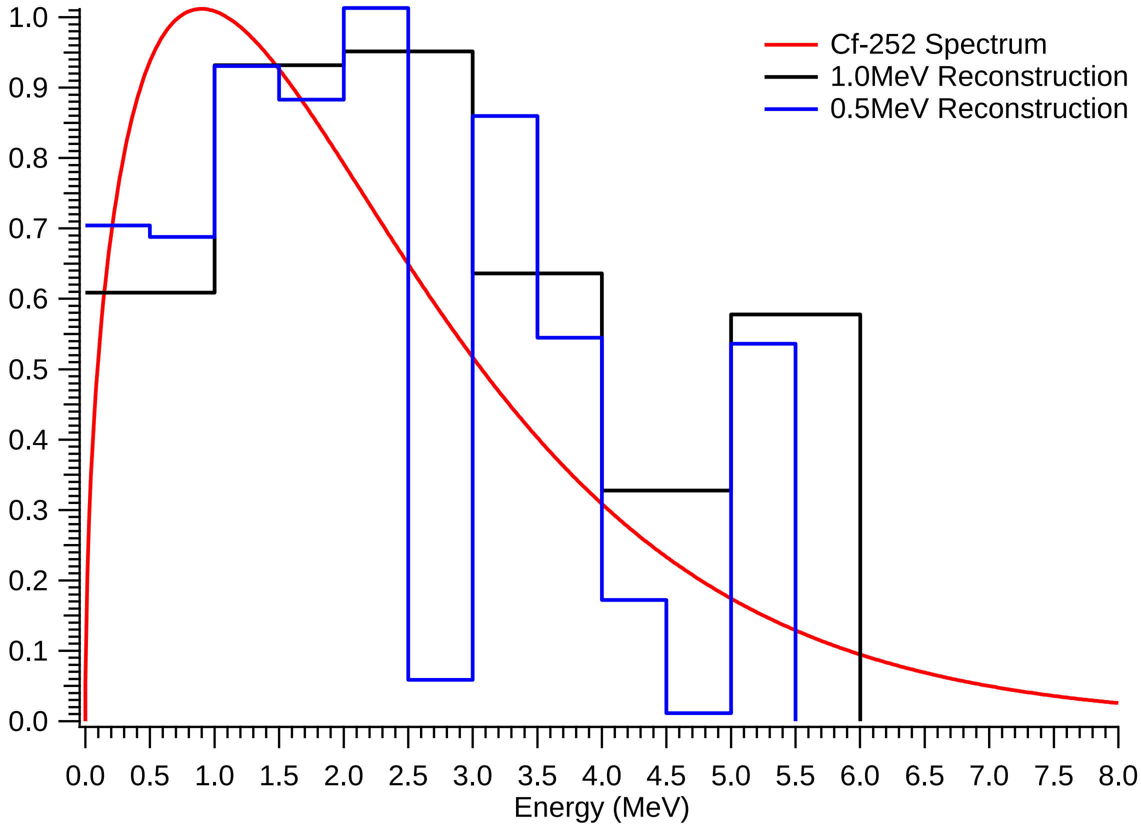

Figure 12: Comparison of the theoretical neutron spectrum for a ^{252}Cf source and the unfolded neutron spectra developed using 0.5-MeV and 1.0-MeV steps.

CHAPTER 4 – Response Function Development

4.1 Detector Design

The next step was to validate the method using experimental response functions. In order to do this, it was first necessary to design and build the detector for data collection. The detector was assembled using a cylindrical 2 inch by 2 inch EJ-299-33A plastic scintillator (Fig. 13), and a B51B03 PMT manufactured by ADIT technologies (Fig. 14).

Figure 13: EJ-299-33A plastic sctinillator used in detector design.

Figure 14: ADIT B51B03 PMT used in detector design.

The detector casing was machined in two pieces. A cylindrical, aluminum housing was used to prevent ambient light from reaching the PMT and affecting the detector output (Fig. 15). An additional aluminum cap was machined to encapsulate the plastic scintillator material (Fig. 16).

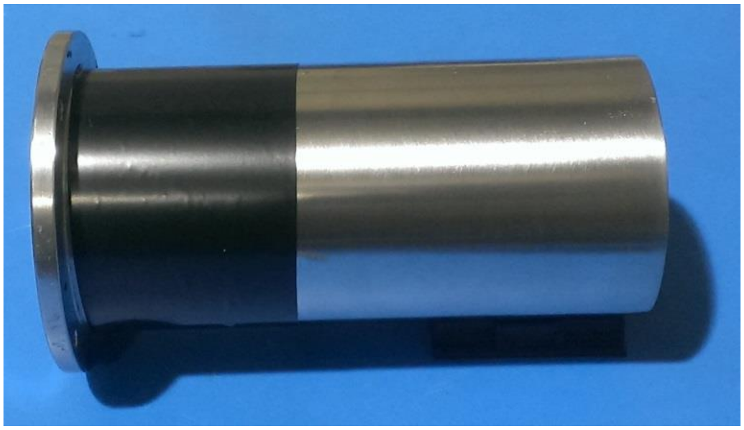

Figure 15: Aluminum body for the PMT.

Figure 16: Aluminum cap for the scintillator material.

The optical grease was applied between the surface of the PMT and scintillator to provide an air tight seal and aid in scintillation light transmission. The cap and cylinder were secured together using four screws (Fig. 17). A ten dynode positive HV base was attached to the PMT to provide transmission of the scintillation light data between the detector and computers. This base was connected to an eMorpho data acquisition unit (Fig. 18), via the HvBase port.

Figure 17: Assembled detector unit, with attached HVC base for signal output.

Figure 18: Emorpho unit used in measurements.

The Emorpho digitizer (Bridgeport Instruments) was used to process the data collected during measurements. The Emorpho also acted as a digital multi-channel analyzer (MCA), processing the scintillator light pulses and producing the energy spectrum for a given source object which was then sent to the computer through the USB channel. It was programmed to perform pulse shape discrimination, and to provide list mode data acquisition options. The list mode capabilities made it possible to record the partial integration time (PIT) of the signal waveform, time, and energy (the total integral under the signal waveform) of each scintillation event while performing measurements.

The detector, with associated digital electronics, was tested using two gamma-ray sources, ^{137}Cs and ^{60}Co. The energy distributions were generated revealing the key features of each response. As shown in Fig. 19 and Fig. 20, the spectra reported by the Emorpho software required calibration of the data bins. Data collected by the detector was treated by Igor Pro to report the response as counts vs. 4096 MCA bins. It was possible to calibrate the values of the MCA bins to report the actual energy values in keVee, as detailed in other publications [61,62]. Using the correlation between MCA bin numbers and energy values in MeVee, it was possible to plot the spectra with respect to energy rather than the bin number.

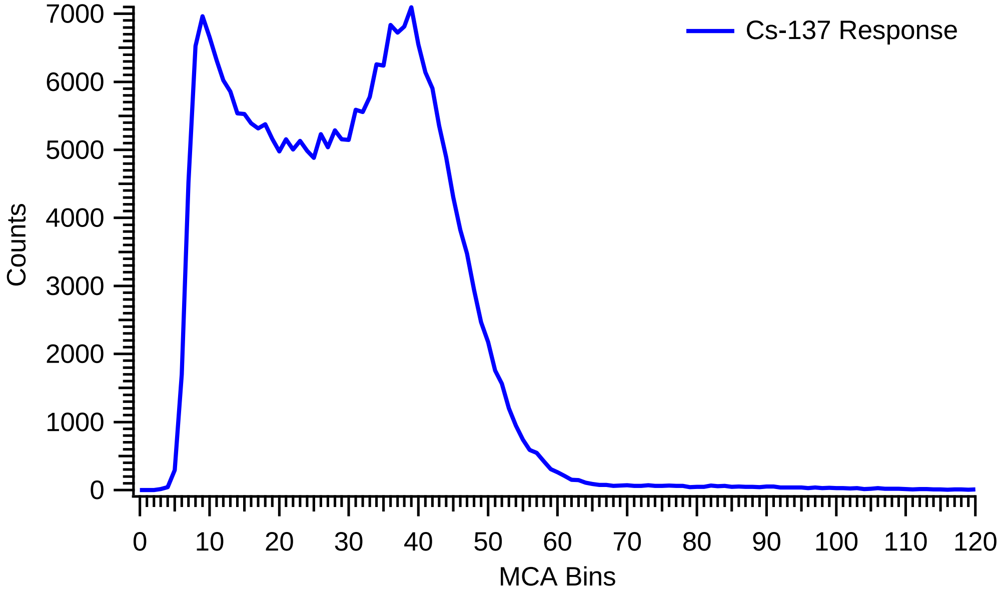

Figure 19: ^{137}Cs response used for calibration.

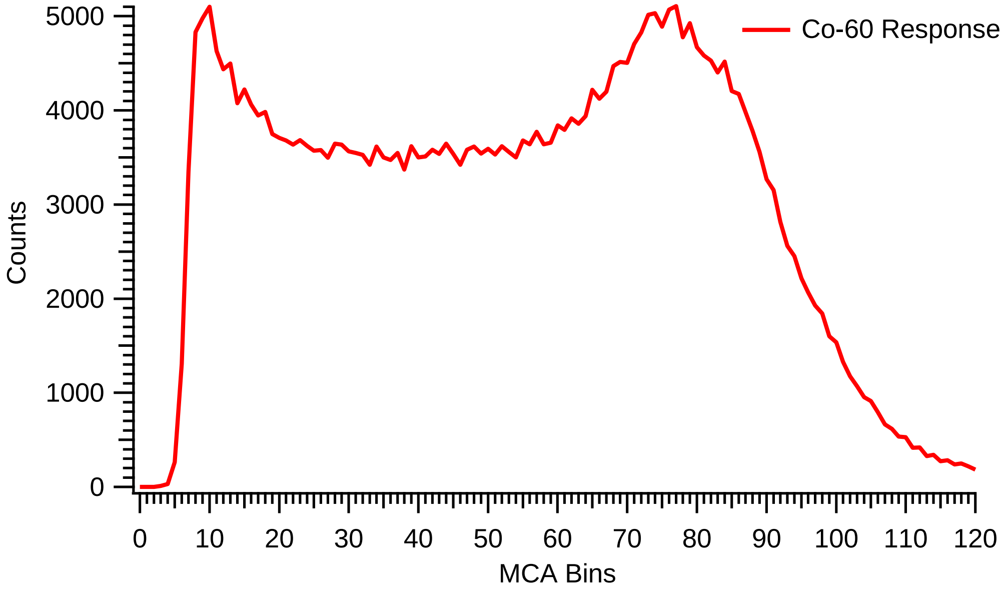

Figure 20: ^{60}Co response used for calibration.

4.2 Response Function Measurement

4.2.1 Experimental Setup

Experimental characterization of the response functions for the EJ-299-33A plastic scintillator was performed at the University of Kentucky's Accelerator Facility. Experimental monoenergetic neutron response functions were collected using the 7-MV Van de Graaff accelerator (see Fig. 21). Although the accelerator could reach 7 MV, the ideal range of operation was 2 MV to 5 MV. The operation outside this range could result in loss of current and beam instability.

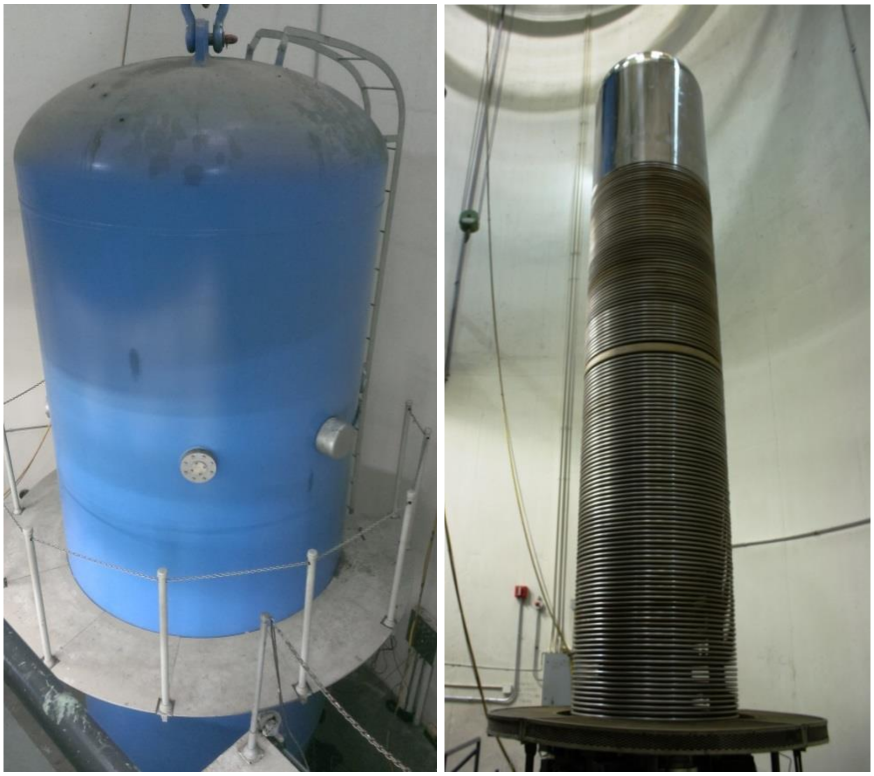

Figure 21: The University of Kentucky's particle accelerator with and without the protective covering that gives it its name.

Available neutron-producing reactions and voltage limitations of the accelerator equipment prevented the measurement of neutron response functions between 8.2 MeV and 12.2 MeV. As a result, data collection was done in energy ranges from 0.1 MeV to 8.2 MeV and 12.2 MeV to 20.2 MeV. By selecting the appropriate reaction and incident charged particle energy, it was possible to do measurements for neutron energies within these ranges with steps as small as 0.1 MeV.

The charged particles were transported along several meters of the beamline, to a gaseous neutron-generating target in the center of the shielded vault shown in Fig. 22 and Fig. 23. The EJ-299-33A scintillator detector was placed in the center of copper shielding, supported by an adjustable frame, which was positioned on top of a base that could be rotated around the target in a 150° arc. The copper shielding was used to reduce the neutron scattering into the detector off of the walls and other objects in the vault. The PSD capability of the detector was adequate in handling the impact of photons produced in the surrounding copper.

The position of the copper shielding on the frame was also adjustable. The blue frame supporting the shielding was placed on wheels and could be moved along the rails of the base to position it closer or farther from the target. This feature was necessary during measurements in order to avoid both extremely low count rates and extremely high count rates. When the count rate peaked above 30,000 counts per second, the copper shielding was moved away from the target to prevent saturation of the detector with pulses. Similarly, when the count rate fell below 3,000 counts per second, the shielding was moved along the base to be closer to the target.

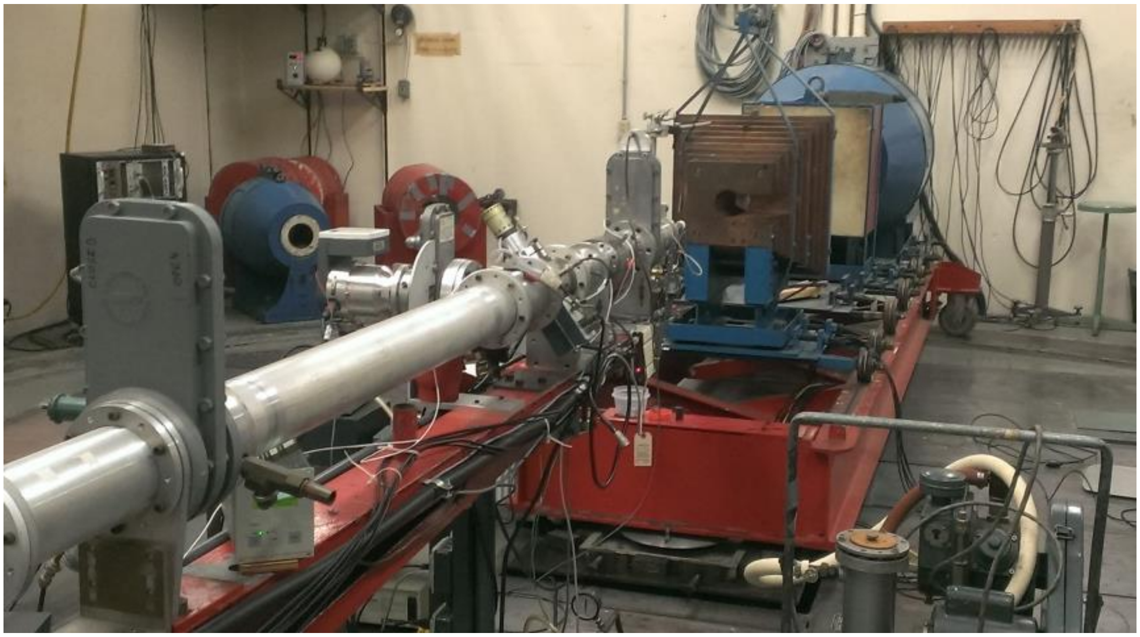

Figure 22: Measurement setup with beamline and detectors; 0° orientation.

Figure 23: Measurement setup with beamline and detectors; 120° orientation.

The central cut-out in the copper shielding was aligned with the axis of the accelerator beamline (Fig. 23). The detector and shielding rested on a rolling base which could be rotated around the center of the room on a raised track. This central point was located directly beneath the accelerator target. Ideally the system was designed for 360° of rotation about the accelerator target, but the physical limitations of the frame and the structural support for the beamline made it possible only to move the frame through 150° of the rotation (Fig. 24). Beyond 150°, the frame which held the detector and shielding came in contact with the structural support provided for the accelerator beamline.

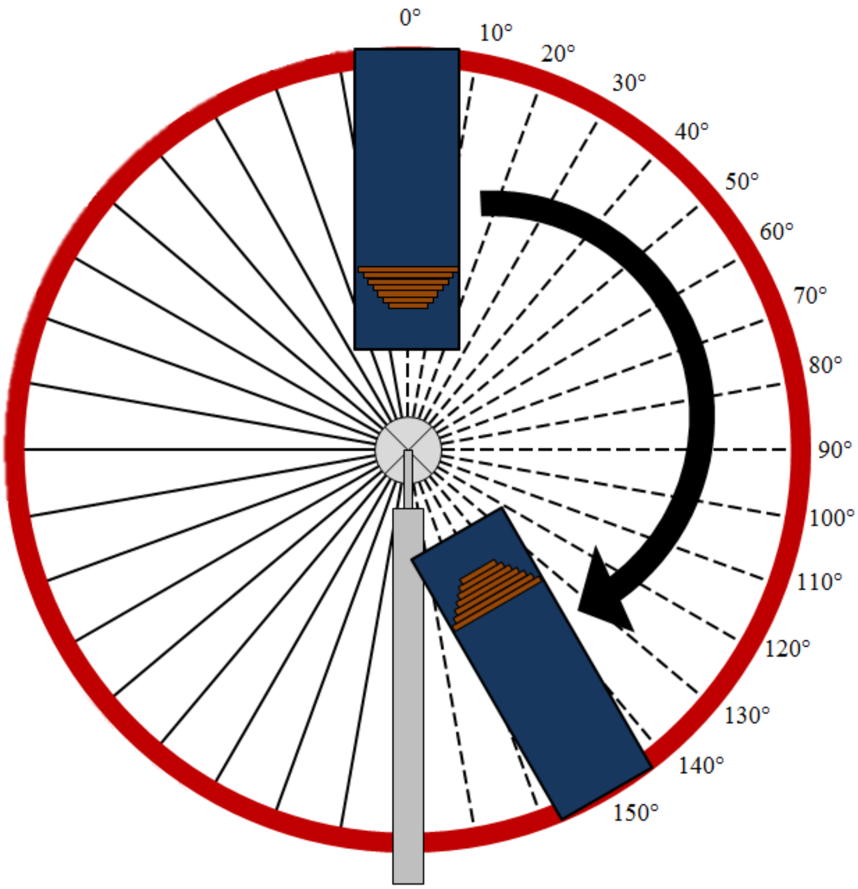

Figure 24: Range of possible motion for the detector system (top view).

The angle of rotation for each measurement was determined using the metal disc positioned under the pivot point of the frame. The disc was marked with 1° increments, and its center was aligned with the center of the accelerator target to provide an accurate reading of the angle at which the detector frame was positioned. The angle of the frame during measurements was used in determining the neutron energy value identified by each recorded response function.

4.2.2 Measurement and Processing of Response Functions

It was possible to use the T(p,n)^{3}He, D(d,n)^{3}He, and T(d,n)^{4}He reactions separately to produce monoenergetic neutrons [63]. Since the stable, recommended range for this accelerator was limited between 2 MV and 5 MV, it was necessary to use all of the available reactions to measure the desired set of monoenergetic neutron response functions.

For the T(p,n)^{3}He reaction (Eqn. 15), tritium gas was used in the target cell. The protons were accelerated down the accelerator coil and transported through the beamline towards the target cell.

$$^{3}H + p \rightarrow {}^{3}He + n \tag{15}$$

The resulting interactions produced monoenergetic neutrons with an energy that was dependent on the voltage of the accelerator (the proton energy). The T(p,n)^{3}He reaction had a Q-value of -0.764 MeV. Using the 2 MV to 5 MV range the accelerator could easily achieve, it was possible to generate proton beams with energies of 1.8 MeV and 4

MeV. These proton energies allowed for the measurement of neutron response functions between 0.1 MeV and 3.2 MeV for different orientations of the incident charged particle beam and the detector.

$$E_n = E_p - 0.764 MeV \tag{16}$$

For the D(d,n)^{3}He reaction (Eqn. 17), deuterium gas was used in the target cell, while deuterons were accelerated down the accelerator coil and transported along the beamline towards the target cell.

$$^2H + {}^2H \rightarrow {}^4He + n \tag{17}$$

The Q-value for this reaction is 3.269 MeV, which when considered with the acceptable accelerator range of 2 MV to 5 MV, meant that it was possible to measure monoenergetic neutrons with energies between 5.27 MeV and 8.27 MeV (Eqn. 18).

$$E_n = E_d + 3.269 MeV \tag{18}$$

The accelerator was tuned to produce deuteron beams with energies of 3.5 MeV, 4.5 MeV, and 5 MeV. These energy choices made it possible to measure monoenergetic neutron response functions between 3.3 MeV and 8.2 MeV for different orientations of the incident charged particle beam and the detector.

For the T(d,n)^{4}He reaction (Eqn. 19), deuterons were accelerated and transported along the beamline towards the target cell of tritium gas.

$$^{3}H+{}^{2}H\rightarrow {}^{4}He+n \tag{19}$$

The Q-value for this reaction is 17.59 MeV, which when considered with the acceptable range of 2 MV to 5 MV, made it possible to measure monoenergetic neutron beams with maximum energies between 19.59 MeV and 22.59 MeV (Eqn. 19). The accelerator was tuned to produce a deuteron beam with an energy of 3.5 MeV in order to measure the monoenergetic neutron response functions between 12.2 MeV and 20.2 MeV.

$$E_n = E_d + 17.59MeV \tag{20}$$

To collect multiple monoenergetic neutron response function data for each reaction and accelerator energy combination the effect of angular distribution on neutron energy was used. Assuming neutrons produced by the proton beam were emitted from the target cell with a given orientation defined with respect to the beamline (*θ*), it was possible to calculate the energy of neutrons emitted at different angles using the differential cross-sections [63]:

$$\frac{d\sigma}{d\omega}(\theta)=\frac{d\sigma}{d\omega}(0^{\circ})\sum_{i}A_iP_i(\theta) \tag{21}$$

Based on the effect of the angular distribution for angles between 0° and 150°, it was possible to determine the energies for individual monoenergetic neutron responses. The resulting energies for the measured monoenergetic neutron responses are recorded in Table 2 [63].

Table 2 – Monoenergetic neutron sources [63].

Nuclear Reactions					
T(p,n)^{3}He	T(p,n) ^{3}He	D(d,n) ^{3}He	D(d,n) ^{3}He	D(d,n) ^{3}He	T(d,n) ^{4}He
Incident Charged Particle Energy					
1.8 MeV	4.0 MeV	3.5 MeV	4.5 MeV	5.0 MeV	3.5 MeV
Neutron Energies					
0.121 MeV	0.696 MeV	3.319 MeV	7.014 MeV	7.868 MeV	12.197 MeV
0.167 MeV	0.723 MeV	3.449 MeV	7.230 MeV	8.029 MeV	12.352 MeV
0.217 MeV	0.833 MeV	3.536 MeV	7.413 MeV	8.146 MeV	12.530 MeV
0.293 MeV	0.936 MeV	3.628 MeV	7.560 MeV	8.241 MeV	12.730 MeV
0.360 MeV	1.067 MeV	3.765 MeV	7.667 MeV		12.953 MeV
0.399 MeV	1.143 MeV	3.861 MeV	7.754 MeV		13.197 MeV
0.440 MeV	1.228 MeV	4.005 MeV			13.462 MeV
0.532 MeV	1.321 MeV	4.104 MeV			13.747 MeV
0.631 MeV	1.421 MeV	4.253 MeV			14.050 MeV
	1.529 MeV	4.406 MeV			14.370 MeV
	1.644 MeV	4.508 MeV			14.705 MeV
	1.766 MeV	4.765 MeV			15.054 MeV
	1.893 MeV	5.022 MeV			15.414 MeV
	2.024 MeV	5.275 MeV			15.782 MeV
	2.158 MeV	5.521 MeV			16.157 MeV
	2.292 MeV	5.755 MeV			16.534 MeV
	2.425 MeV	5.972 MeV			16.911 MeV
	2.555 MeV	6.171 MeV			17.285 MeV
	2.679 MeV	6.345 MeV			17.651 MeV
	2.795 MeV	6.493 MeV			18.006 MeV
	2.901 MeV	6.612 MeV			18.346 MeV
	3.074 MeV	6.698 MeV			18.668 MeV
	3.184 MeV	6.768 MeV			18.968 MeV
					19.242 MeV
					19.487 MeV
					19.700 MeV
					19.878 MeV
					20.019 MeV
					20.121 MeV
					20.204 MeV

Measurements for each of the monoenergetic energies listed in Table 2 were recorded for 220 buffers. The cutoff was based on buffers instead of time to make normalization unnecessary between responses. Count rates were reported in the range of 3,000 to 30,000 counts per second, with the average count rate remaining around 6,000 counts per second. These measurements consisted of individual pulses recorded by the EJ-299-33A detector, which were transmitted through the Emorpho unit to a computer running Igor Pro software. Response functions were collected using the list mode which allows for the time, energy, and partial integral value to be recorded for each pulse generated by the detector. This particular mode was selected because it provided the partial integral values for each pulse, which were the basis for performing pulse shape discrimination. The PID value was a ratio based on the integration time (IT) and partial integration time (PIT) of a given pulse (Fig. 25). Integration time was defined by the duration of the pulse, and the partial integration time was a user-defined value.

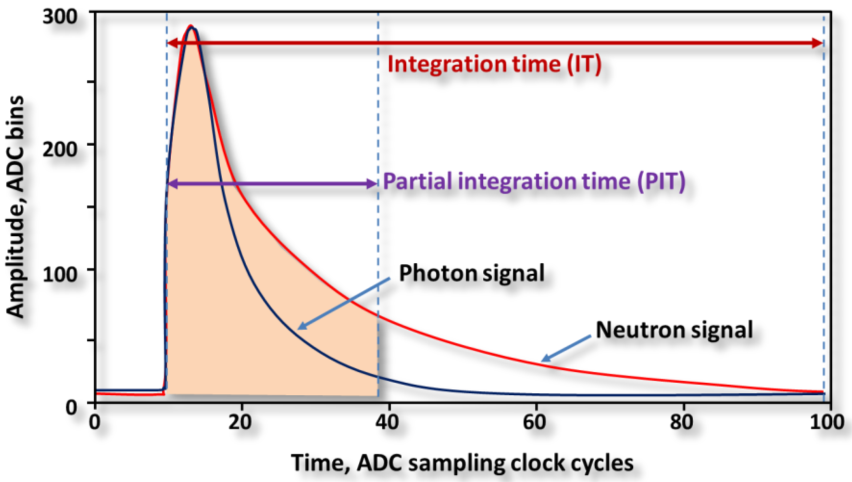

Figure 25: Comparison of neutron and photon signals for development of PID value .

The PID value for a pulse was defined as the ratio of the “tail” integral to the “head” integral (Eqn. 22). For the purposes of this research, the “head” integral is defined as the area under the curve between the start of the pulse and the PIT value. In Fig. 25, the signals are plotted in terms of ADC clock cycles instead of standard time units. Igor Pro defines an ADC clock cycle as being equivalent to 12.5 nanoseconds. For the example shown in Fig. 25, the start of the pulse occurred at 10 clock cycles (125 nanoseconds), while the PIT value was assigned a value of 40 clock cycles (500 nanoseconds). The “tail” integral is the difference between the integral of the IT value and the integral of the PIT value, making the PID value dependent on the “tail” of the signal. Since neutrons required more time to lose energy than photons, the signals produced by them had longer tails than for photons, correlating directly to the larger PID values. This differentiation was used in PSD, which focuses on distinguishing between the signal waveforms of neutrons and photons.

$$PID = \frac{IT - PIT}{PIT} \tag{22}$$

Although the charge particle beam was configured to produce monoenergetic neutrons in the target cell, it was still possible for the detector to record both neutron and photon pulses as the part of the response function. As a result, it was necessary to implement a PSD procedure using the Igor Pro interface. This procedure was designed to isolate the neutron portion of the total recorded response function using a PID cutoff value. The PID value of each recorded pulse was compared to the cutoff PID value, those pulses with PID values below the cutoff were discarded (photon pulses), and those pulses with PID values greater than or equal to the defined PID value were used to develop a neutron response function. This was repeated for each monoenergetic response function measured. In general this resulted in the development of response functions with lower magnitudes and slightly different features than the total response function initially measured. Fig. 26 shows a comparison of the differences between the total response function (neutron and gamma pulses combined), the isolated neutron response function, and the discarded gamma response function.

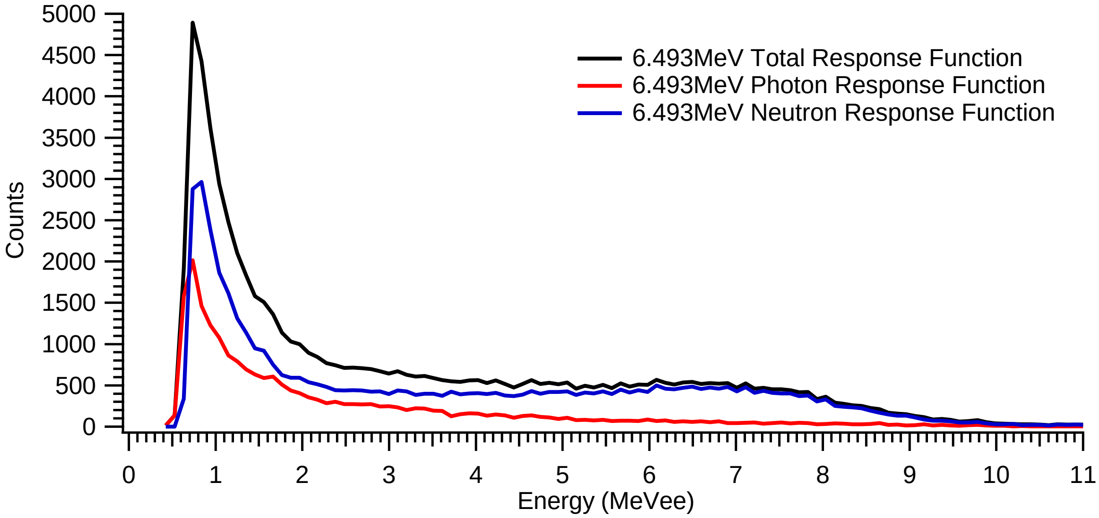

Figure 26: Comparison of total response function measured for a 6.493-MeV neutron beam with it’s neutron-only and gamma-only component response functions.

As expected, the removal of the photon pulses from the response function reduced the magnitude of the neutron response function. This processing did not significantly alter the shape of the response function at the higher energies (4 MeVee to 9 MeV) where the features could be used to identify specific monoenergetic neutron beams. Plotting these response functions together provided a visualization of the unique features and how they change with respect to the source energy used. The result of this is shown in Fig. 27. The monoenergetic response functions were plotted for source energies between 0.617 MeV and 8.241 MeV. This selection was chosen for the discrimination it showed. For source energies below 0.5 MeV, the EJ-299-33A scintillator showed limited discrimination ability to between neutrons and photons. At higher energies, the counts per bin were too low in magnitude to show clear discrimination when plotted against response functions with peak counts above 10,000.

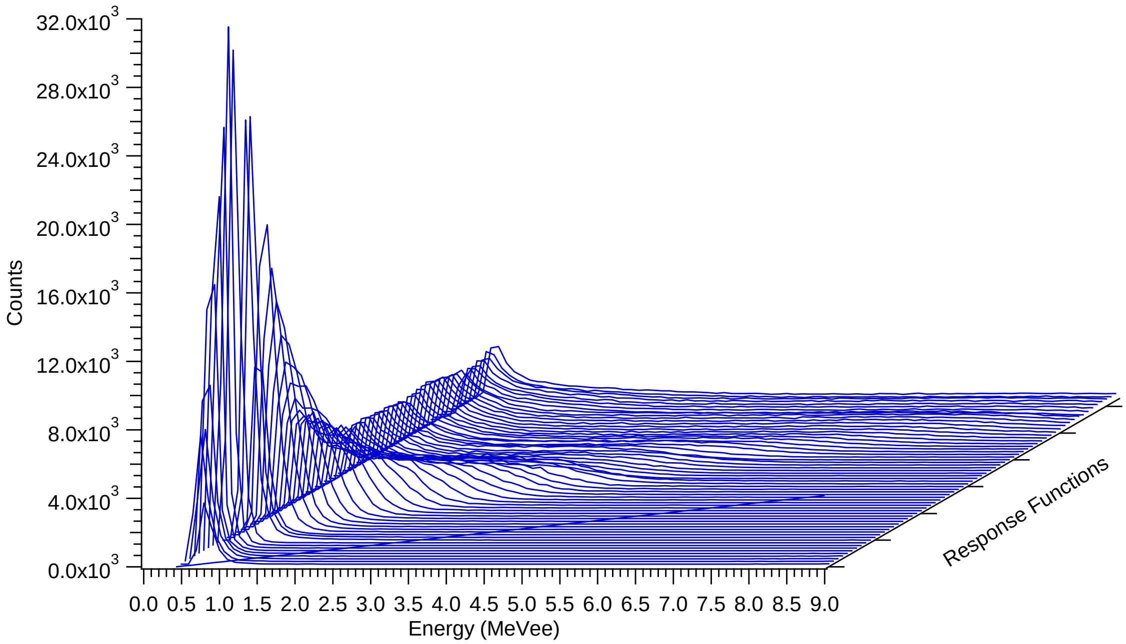

Figure 27: Surface plot of the monoenergetic response functions collected between 0.617 MeV and 8.241 MeV.

A surface plot was also created for response functions between a range of 1.893 MeV and 8.241 MeV. The result is included below in Fig 28, the restriction of the response functions made it possible to see the impact of source energy on the shape of the response function with greater clarity. As expected, two trends appeared when the energy of the incident particles was increased. The first occurred during data processing, as the source energy was increased, greater discrimination could be seen between the photon and neutron portions of the recorded response functions. The second, which was visible in both surface plots (Figs. 27 and 28), is the spreading of the response function as higher energy neutrons pass through the scintillator cell, depositing more energy.

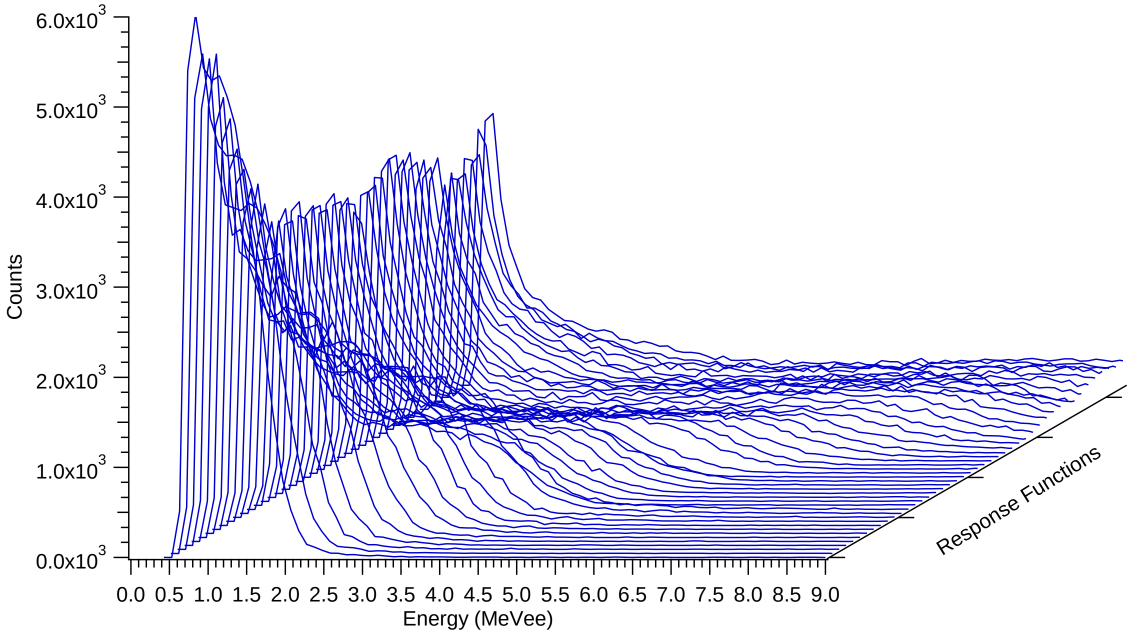

Figure 28: Surface plot of the monoenergetic response functions collected between 1.893 MeV and 8.241 MeV.

4.3 Plutonium-Beryllium Source

4.3.1 Experimental Setup

Experimental response data were collected using the 2-Curie plutonium-beryllium (PuBe) isotopic neutron source at the University of Nevada, Las Vegas (Fig. 29). The 32-gram source was a homogenous mixture of ^{239}Pu and ^{4}Be sealed in a stainless steel vessel, and stored inside a 55-gallon drum [64].

Figure 29: The plutonium-beryllium source at the University of Nevada, Las Vegas.

PuBe response measurements were carried out with the same EJ-299-33A scintillator detector that was used in collecting the monoenergetic neutron response functions at the UKAL facility. The detector was placed 30 cm away from the beam port on the drum, as indicated in Fig. 29. The white safety plug shown in Fig. 29 and Fig. 30 was removed during measurements. The face of the detector was positioned such that the center of the scintillator material was coincident with the center of the beam port.

Figure 30: Experimental setup of the plutonium-beryllium source and EJ-299-33A detector.

4.3.2 Measurement and Processing of Plutonium Beryllium Responses

Measurements of the PuBe response were performed using 220 buffers (Fig. 31). This measurement cutoff was selected for consistency with the monoenergetic response function measurements. The general features of the responses showed similar trends, with a major peak near 0.75 MeV, and additional features appearing at 2.5 MeV, and 4 MeV. It should be noted, that the data presented here do not reflect the response of a bare PuBe source. Measurements were taken using the setup detailed above, where the PuBe source was moderated by the surrounding drum.

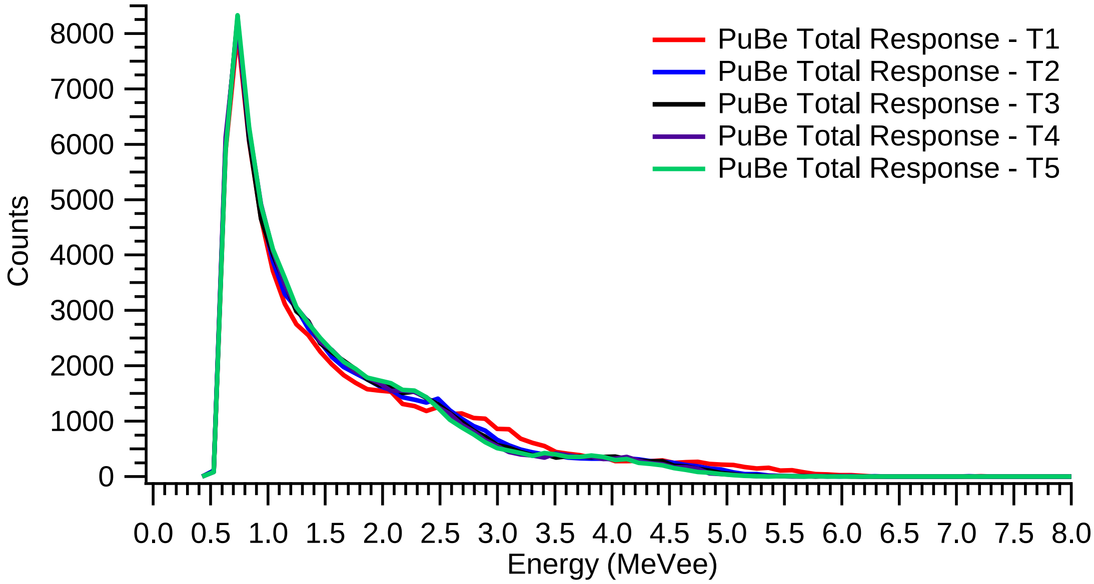

Figure 31: Several PuBe responses, as measured by the EJ-299-33A scintillator.

Like the response functions collected from the UK accelerator, the PuBe responses recorded at UNLV reported a combination of neutron and photon counts. This made separation of these components necessary prior to performing the spectral unfolding technique. The Igor Pro procedure for performing pulse shape discrimination on the response functions was used to perform the same task for each of the recorded PuBe responses. Fig. 32 shows an example of the effect this separation had on the response used in the unfolding procedure. Unlike the monoenergetic response functions from the accelerator, the ratio of neutron to photon counts in the PuBe responses was considerably lower. The significant difference between the magnitudes of the photon and neutron responses was expected since PuBe sources produce neutrons in addition to a significant quantity of photons.

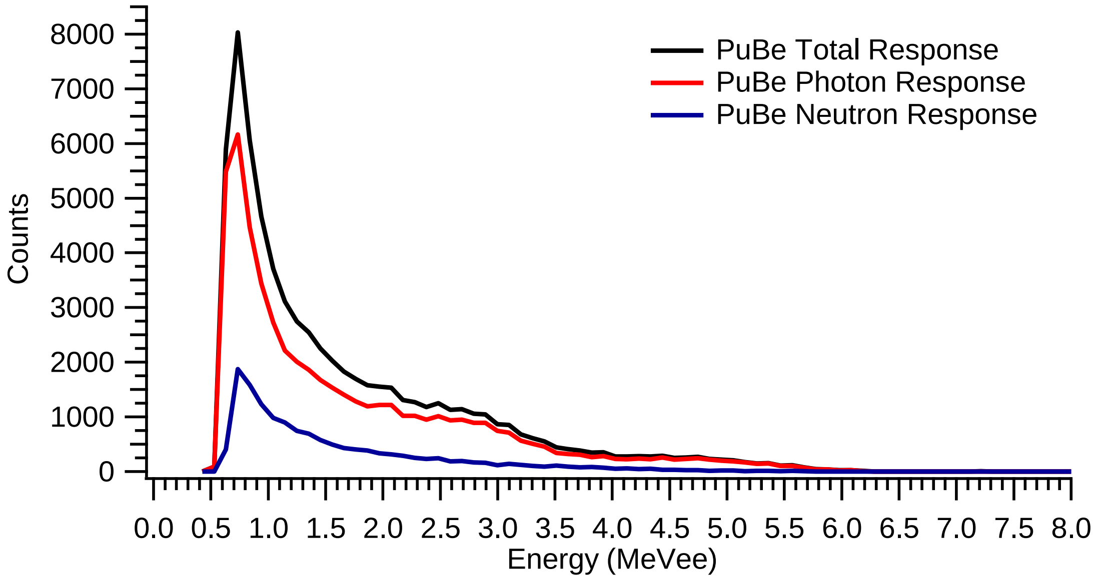

Figure 32: Polyenergetic PuBe response separated into neutron and photon components.

A figure of merit (FOM) analysis was also completed for the pulse shape discrimination of the PuBe source. This was done to verify that the method was performing within reasonable limits. Fig. 33 shows a plot of the PID values against the particle energy for each pulse. The differentiation between neutron and photon signals is obvious, with the neutron arm of the plot having a higher range of PID values (0.25-0.5) than the photons (0.0-0.25). The PID data was also graphed in Fig. 34, using the number of counts vs. the PID value. The resulting data was then used to determine the FOM of the pulse shape discrimination data using the relationship in the figure. Based on the width of the photon peak (W1), the width of the neutron peak (W2), and the separation between each peak, and FOM of 1.3 was calculated. Each peak was identified using the maximum count value for that peak. The widths were then determined at the point of the full width half maximum (FWHM) of each peak. This resulted in an FOM of 1.3.

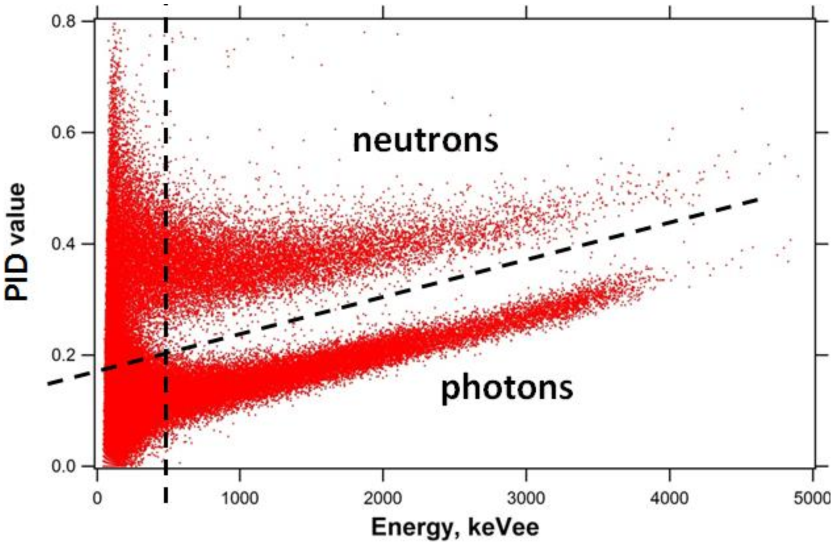

Figure 33: PID values for polyenergetic response of PuBe.

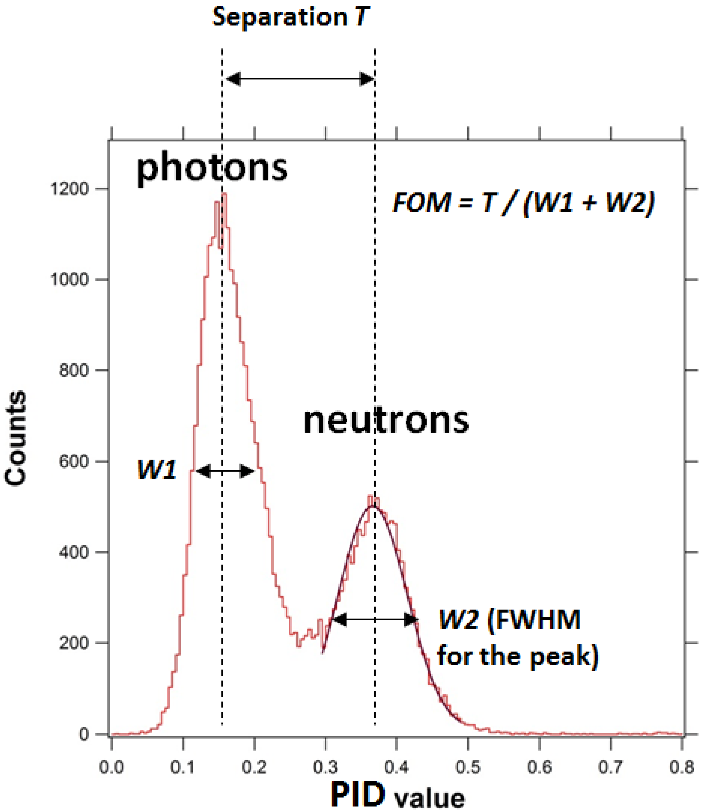

Figure 34: Figure of merit analysis for pulse shape discrimination of PuBe response.

CHAPTER 5 – RESULTS AND DISCUSSION

5.1 Spectral Unfolding Results for PuBe

Experimental verification of the spectral unfolding technique was carried out using the monoenergetic neutron response functions from the accelerator (Fig. 27) and the isolated neutron responses developed from the PuBe measurements (Fig. 35).

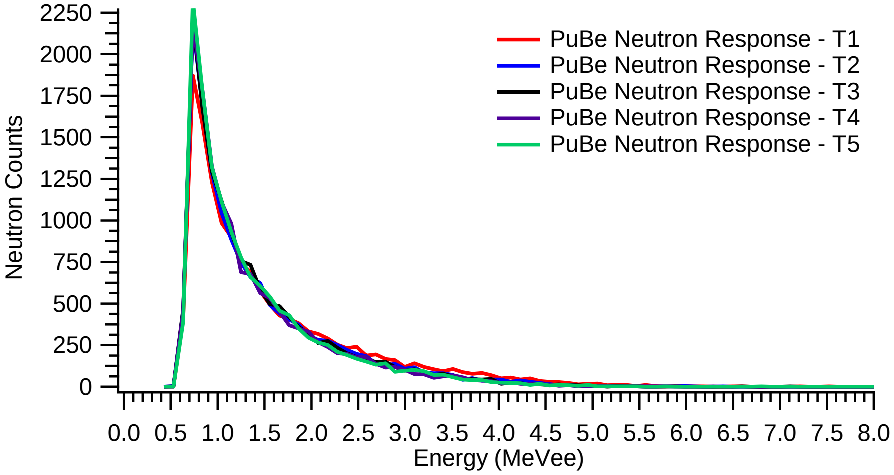

Figure 35: Separated PuBe responses containing only neutrons.

Spectral unfolding was carried out for each of the measurements above using the MATLAB code built for this purpose. The fitting procedure was carried out using the **fmincon** function, with the previously determined initial guess value of 0 for all coefficients. The lower and upper limits for coefficients were also set as 0 and 1 respectively. Using these restrictions, each PuBe measurement was unfolded using response function increments of 0.1 MeV, 0.5 MeV, and 1 MeV as shown in Figs. 38-40.

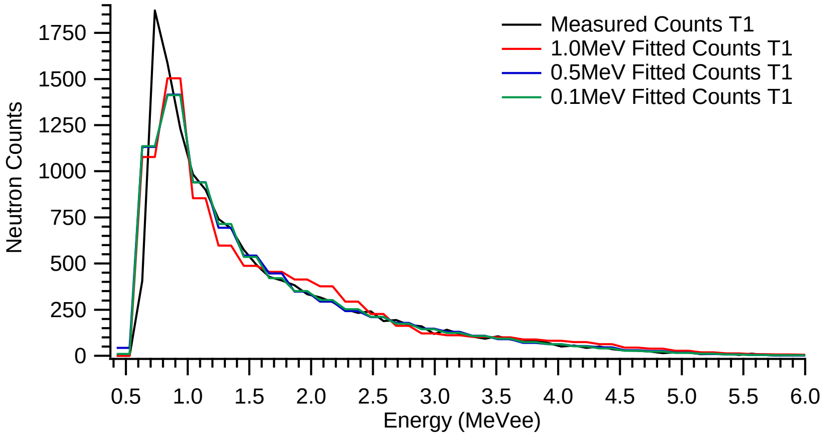

Figure 36: Comparison of fitting results for PuBe measurement 1, using response function increments of 0.1 MeV, 0.5 MeV, and 1 MeV.

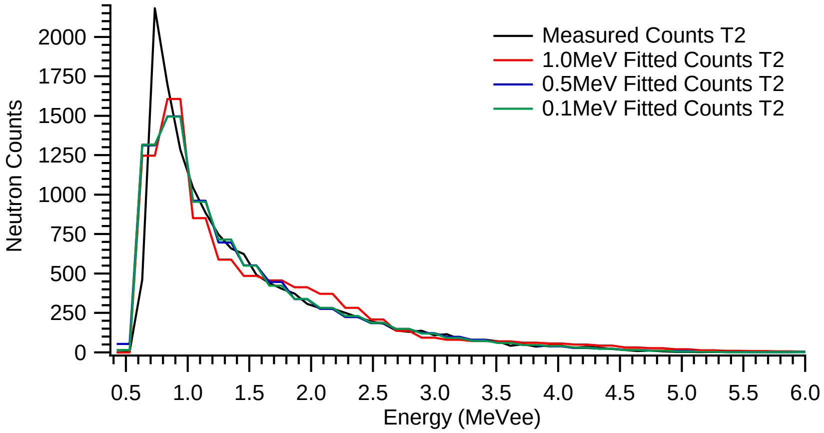

Figure 37: Comparison of fitting results for PuBe measurement 2, using response function increments of 0.1 MeV, 0.5 MeV, and 1.0 MeV.

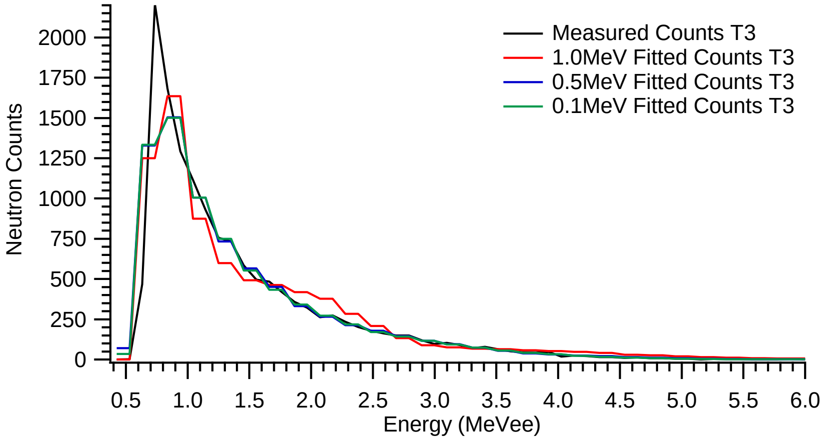

Figure 38: Comparison of fitting results for PuBe measurement 3, using response function increments of 0.1 MeV, 0.5 MeV, and 1.0 MeV.

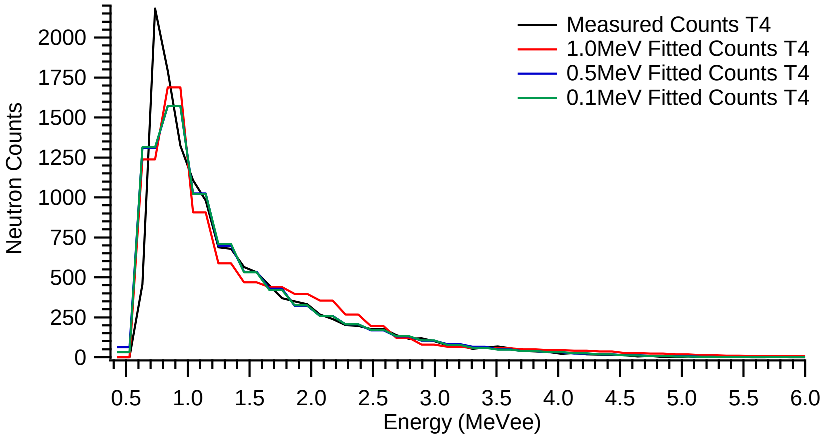

Figure 39: Comparison of fitting results for PuBe measurement 4, using response function increments of 0.1 MeV, 0.5 MeV, and 1.0 MeV.

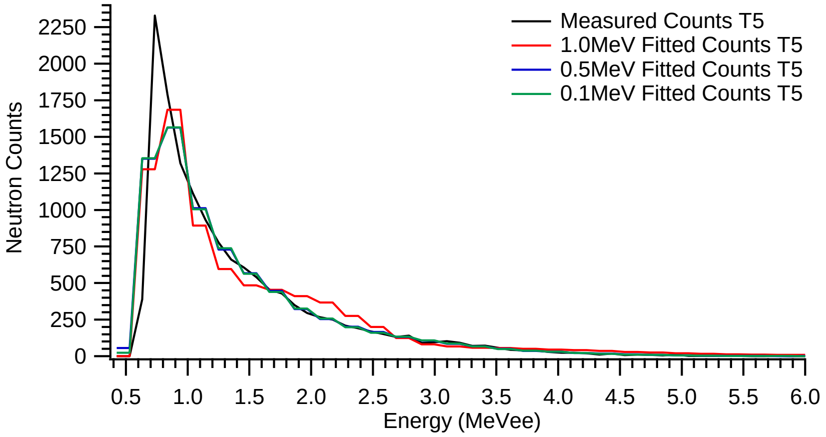

Figure 40: Comparison of fitting results for PuBe measurement 5, using response function increments of 0.1 MeV, 0.5 MeV, and 1.0 MeV.

For each measurement, the 1.0-MeV increment between response functions consistently produced a poorer fit than the use 0.1-MeV and 0.5-MeV increments. The data generated using increments of 0.1 MeV and 0.5 MeV returned almost identical fits, which made both of the use of either of these increments preferable to the 1.0-MeV increment. This was verified by a statistical analysis of the overall fit for each response (Table 3). As indicated, use of the 1.0-MeV increment repeatedly produced poorer quality fits, while 0.5-MeV and 0.1-MeV increments showed with similar accuracy.

Table 3 – Comparison of error of fit for various response function increments.

	PuBe Measurement				
	1	2	3	4	5
Increment	**Error of Fit**				
0.1 MeV	0.6796	0.6491	0.6514	0.6545	0.6228
0.5 MeV	0.6784	0.6481	0.6504	0.6537	0.6221
1.0 MeV	0.6645	0.6328	0.6293	0.6375	0.6049

Final verification of the unfolding technique focused on comparison of the coefficients produced. For each response function increment, several PuBe measurements were unfolded to allow for comparison of increment impact, and to see how the results of multiple measurements from a single source would be handled by each increment set.

The first increment compared a 1.0-MeV step between the response functions, relying on the monoenergetic responses collected between 0.121 MeV and 8.241 MeV. The unfolding procedure was carried out using this increment for 5 measurements of the PuBe response. The resulting coefficients for each measurement are tallied in Fig. 41. In general, the unfolding procedure produced similar coefficients for each PuBe measurement. The step size of the increments made an identifiable reconstruction of the energy spectrum extremely unlikely.

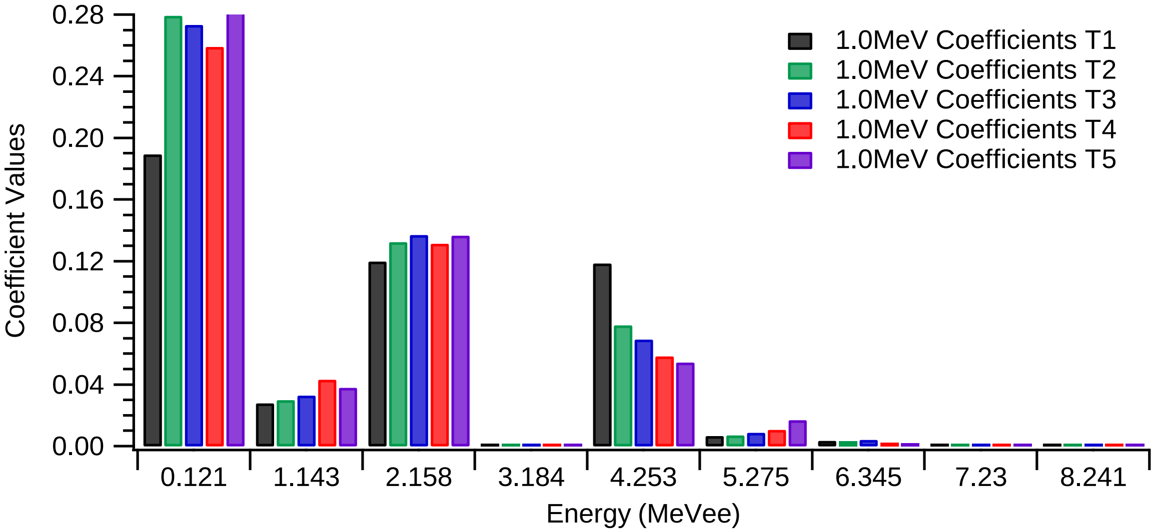

Figure 41: Comparison of coefficients produced for PuBe measurements using a 1.0-MeV step in the unfolding process.

The next increment considered was 0.5 MeV (Fig. 42). The unfolding procedure was carried out using this increment for the same 5 measurements of the PuBe response used to test the 1.0-MeV increment. The resulting set of coefficients produced a more reasonable approximation of the expected energy spectrum for a PuBe source. Unlike the 1.0-MeV increment, the use of a 0.5-MeV increment made it possible to identify peak energies at 1.644 MeV and near 4 MeV.

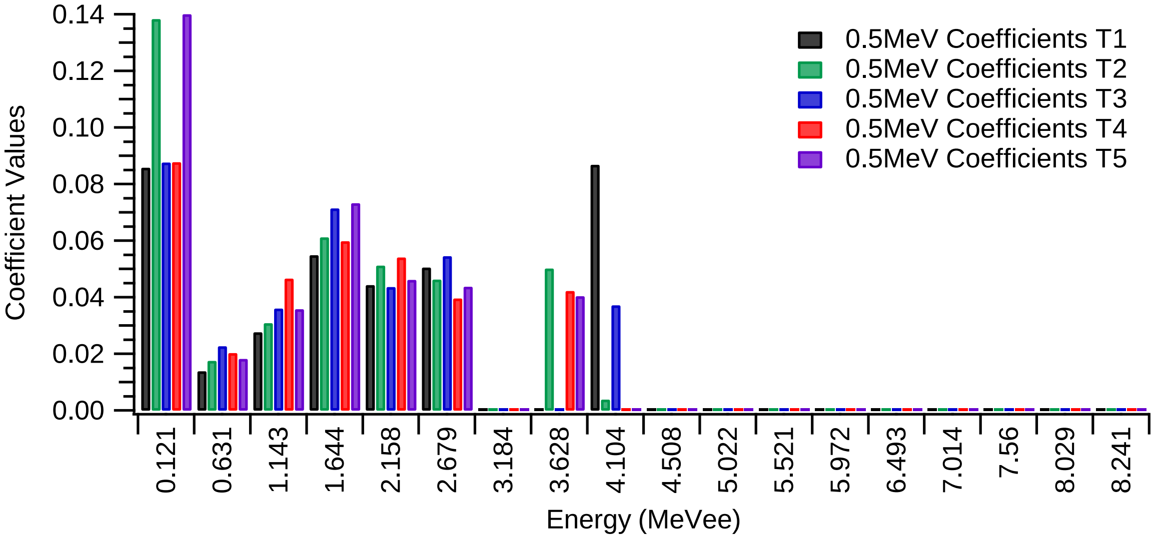

Figure 42: Comparison of coefficients produced for PuBe measurements using a 0.5MeV step in the unfolding process.

The last increment tested was a 0.1 MeV step. The results are tallied in Fig. 43, response functions were used for a range of 0.121 MeV to 8.241 MeV. Coefficient values were only produced between energies of 0.631 MeV and 4.253 MeV, beyond these limits, the unfolding procedure produced coefficients values of 0. Unlike the 0.5-MeV and 1.0-MeV increments, the use of the 0.1-MeV increment produced a discrete set of coefficients at various energies. There is still potential to identify the source based on the unique combination of discrete energies, but the goal of this project was source identification through a spectrum. This made the use of a 0.1-MeV response function increment unsuitable. Additionally, the identification of discrete energies makes the unfolding procedure extremely sensitive to minor deviations in response functions for the same source. Although all 5 PuBe responses were measured using an identical source and detector configuration, a comparison of the coefficients shows the potential for variation in the outcomes. In the figure below, this sensitivity is especially obvious in the variation shown for discrete energies of 1.766 MeV, 2.425 MeV, 2.679 MeV, 2.795 MeV, and 3.184 MeV.

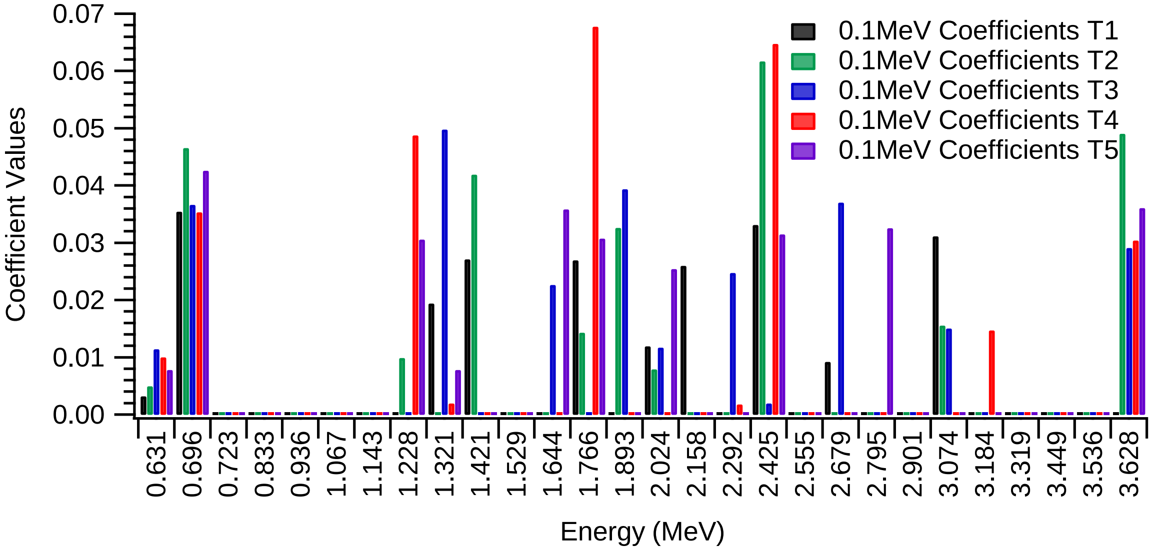

Figure 43: Comparison of coefficients produced for PuBe measurements using a 0.1-MeV step in the unfolding process.

5.2 Spectral Unfolding Results for a DD Source

While the PuBe response verified the ability of the unfolding technique to handle a response from a polyenergetic source, it was also necessary to examine the technique's effectiveness in isolating the response of a monoenergetic fusion source. To this end, the response of a DD source was examined using the unfolding method. The response function measured for a charged particle beam energy of 2.555 MeV was used as the source response. The unfolding technique was attempted using 0.5-MeV and 1.0-MeV increments between the response functions. The resulting fits for each increment are compared with the actual response in Fig. 44. Visual inspection indicated that the 0.5-MeV increment provided a better fit than the 1.0-MeV increment. This was verified by statistical analysis of both fits, which reported fits of 0.95189 and 0.83871 for increments of 0.5 MeV and 1.0 MeV, respectively.

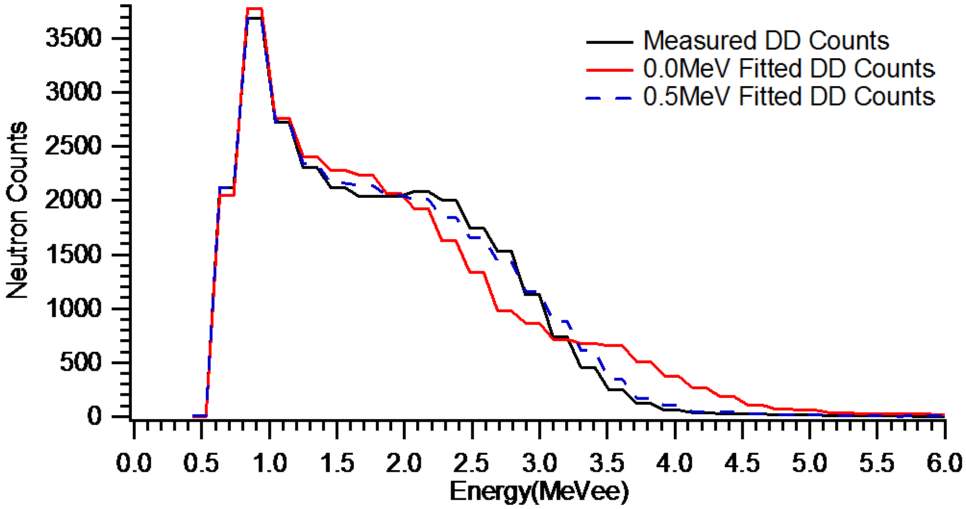

Figure 44: Comparison of fitting results for a DD source, using response function increments of 0.5 MeV and 1.0 MeV.

The coefficients produced by fitting the DD response with a range of response functions between 0.121 MeV and 20.204 MeV are shown in Figs. 45 and 46. As suggested by the statistical comparison of the fitting results, the 0.5-MeV increment was better able to accurately predict the energy of the source. As indicated by the graph in Fig. 45, this was due primarily to the larger number of stored response functions used by the 0.5-MeV increment. By providing a greater variety with which to compare the DD response, it was more likely that the unfolding technique would identify an energy closer to that of the source response. In this case, the unfolding technique identified the source energies as 2.158 MeV and 2.679 MeV with coefficients of 0.2 and 0.8 respectively. Multiplying each coefficient by its energy, and taking the sum produces a source energy value of 2.5748 MeV, which has a mean square error of only 3.92E-4 when compared with the expected energy value of 2.555 MeV.

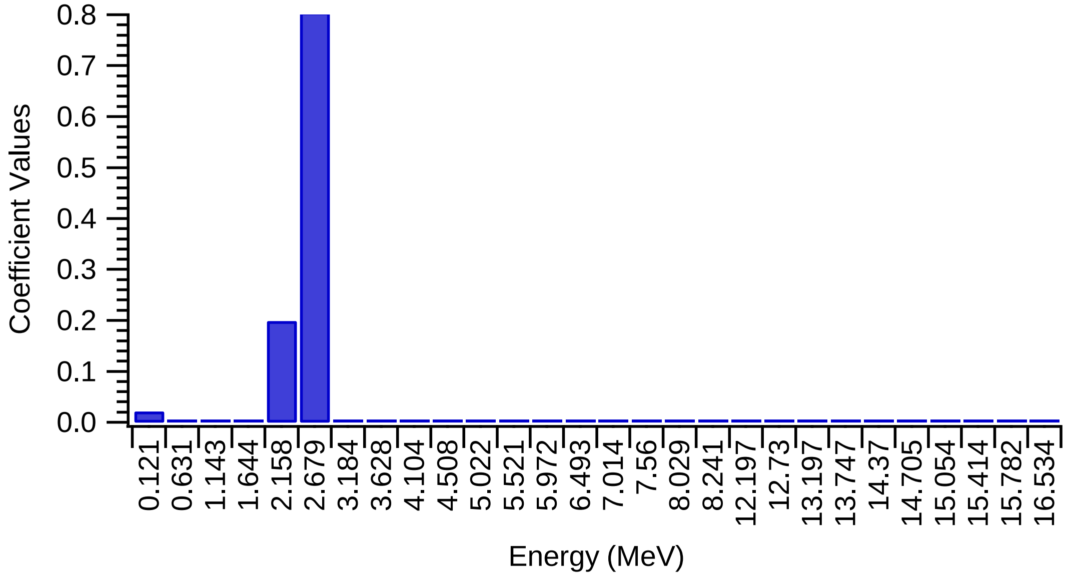

Figure 45: Coefficients produced for a DD source using a 0.5-MeV step in the unfolding process.

The coefficients produced by using a 1.0-MeV increment are shown in Fig. 46. Unlike the results from the 0.5-MeV increment, this data set had fewer responses stored, which directly affected the coefficients produced. For this increment, the unfolding technique identified the source energies as 2.158 MeV and 3.184 MeV with coefficients of 0.53 and 0.51 respectively. Multiplying each coefficient by its energy, and taking the sum produces a source energy value of 2.7676 MeV, which has a mean square error of only 4.519E-2 when compared with the expected energy value of 2.555 MeV. Based on both a statistical analysis of the fits, and of the reported coefficient values, it appeared that the 0.5-MeV increment was preferable for use with the DD response.

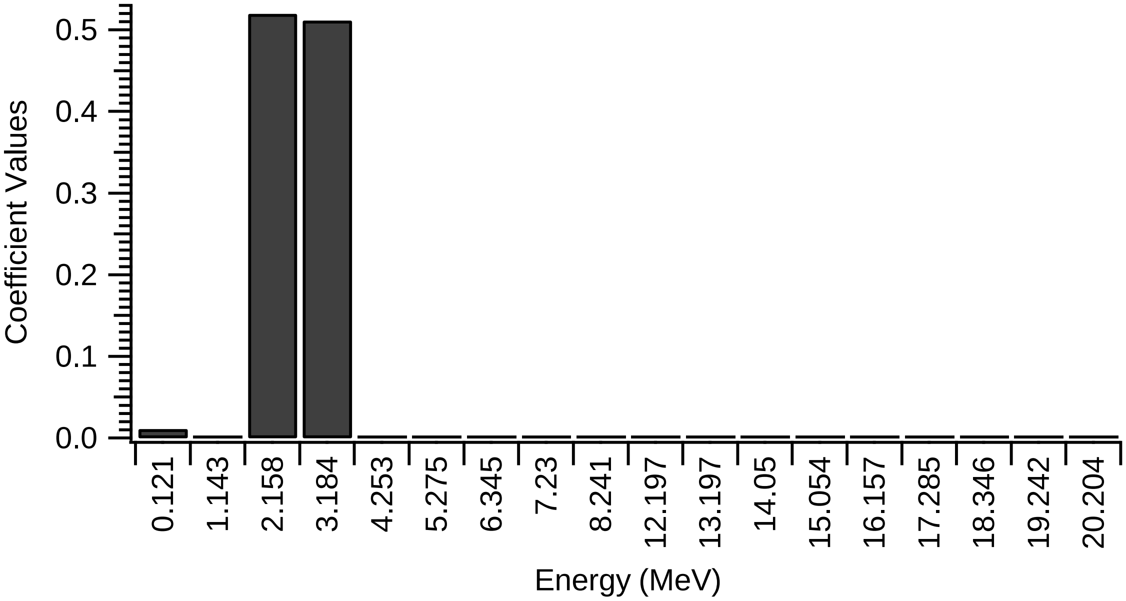

Figure 46: Coefficients produced for a DD source using a 1.0-MeV step in the unfolding process.

5.3 Spectral Unfolding Results for a DT Source

The response of a DT source was also examined using the unfolding technique. The response function measured for 14.050 MeV was used as the source response. As with the DD source, unfolding was attempted with a 0.5-MeV increment, and with a 1.0-MeV increment between the response functions. The resulting fits are compared with the actual response in Fig. 47. Visual inspection indicated that there was no difference in the fits provided by the 0.5-MeV and 1.0-MeV increment. This was verified by statistical analysis of both fits, which reported similar values of 0.97632 and 1.0 for increments of 0.5 MeV and 1.0 MeV respectively.

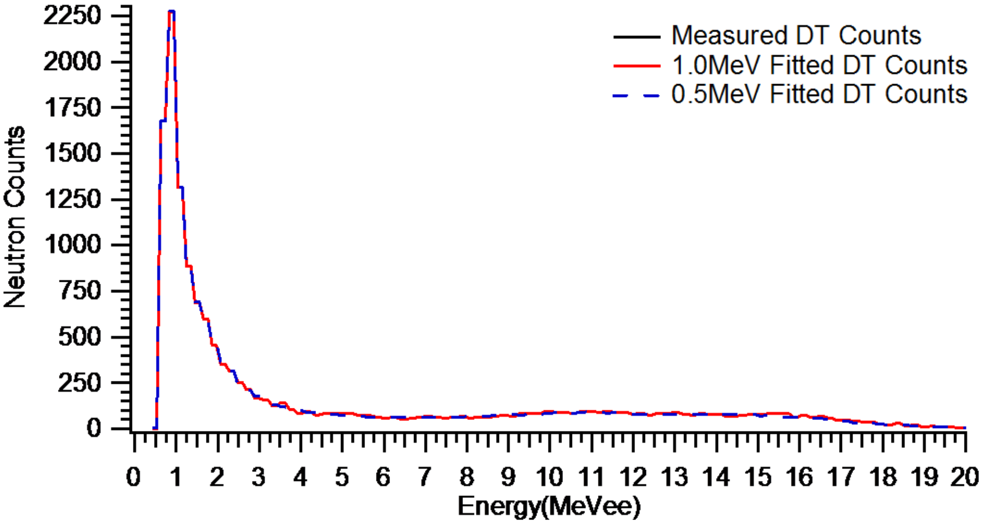

Figure 47: Comparison of fitting results for a DT source, using response function increments of 0.5 MeV, and 1.0 MeV.

Although the fit for the 1.0-MeV increment reported an exact match to the source response, this was not definitive confirmation that this increment was better than a 0.5-

MeV increment. Instead it indicated that the stored response functions for the 1.0-MeV increment specifically included the 14.050-MeV response function, while those stored for the 0.5-MeV increment did not. A comparison of Fig. 48 and Fig. 49 supported this explanation. In both figures, the labels on the x-axis are consistent with the response functions used by each increment option. For the 0.5-MeV increment (Fig. 48), energies of 12.730 MeV, 13.197 MeV, 13.747 MeV, 14.370 MeV, and 14.705 MeV were stored, surrounding the response for 14.050MeV but excluding it. The resulting coefficients for these energies were reported as 0.17, 0.22, 0.22, and 0 respectively. Including the additional coefficient if 0.07 reported for the energy of 15.782 MeV, it was possible to multiply each coefficient of by its respective energy, take the summation and get an overall energy of 13.939 MeV. When compared with the expected 14.050-MeV source energy, the mean square error was only 1.2406E-2.

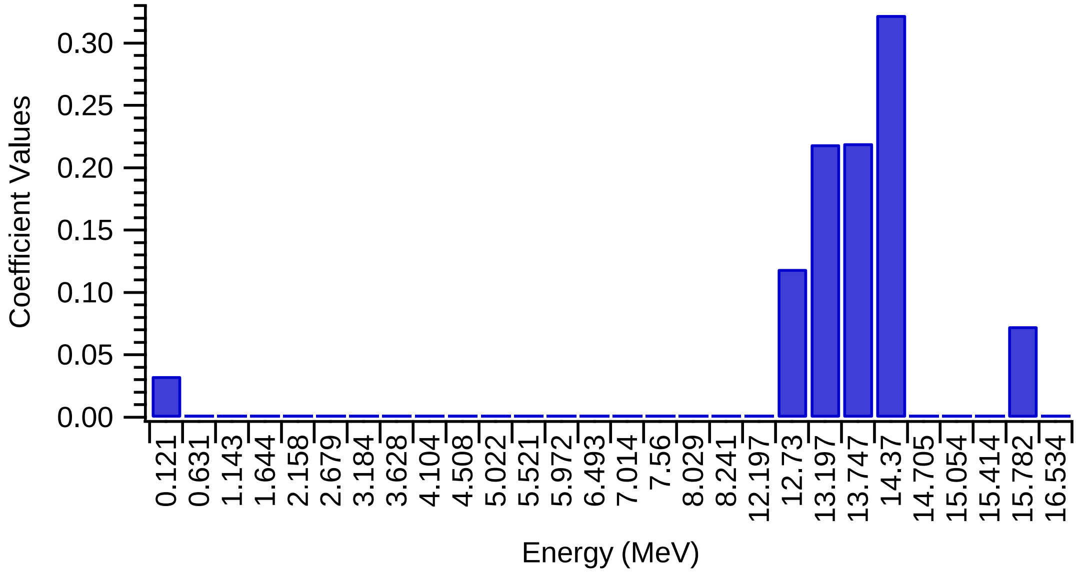

Figure 48: Coefficients produced for a DT source using a 0.5-MeV step in the unfolding process.

For the 1.0-MeV increment (Fig. 49), the assumed response of the DT source (14.05 MeV) was included as one of the responses used for unfolding. As a result of this, the unfolding technique was able to focus on and identify a single response function with a coefficient of 1. Although this was a unique case, it did reveal that the unfolding technique can easily determine the discrete values of those response functions which are stored in its memory.

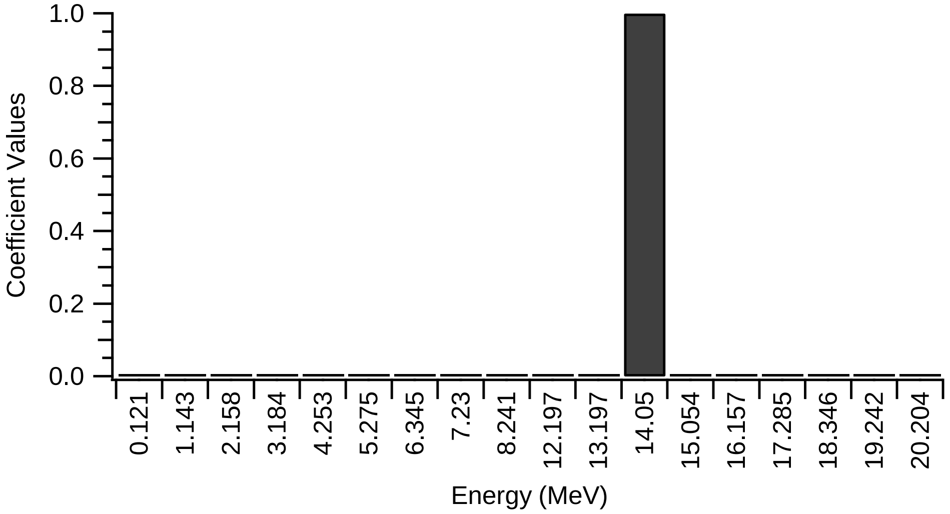

Figure 49: Coefficients produced for a DT source using a 1.0-MeV step in the unfolding process.

CHAPTER 6 – CONCLUSIONS & FUTURE WORK

6.1 Conclusions

The primary goal of this research was achieved. A spectral unfolding technique employing wavelets was developed for use with the EJ-299-33A scintillator. Computational development and experimental verification of the technique were carried out. Post processing procedures and codes were developed for the purposes of carrying out pulse shape discrimination and for performing the actual spectral unfolding process. Optimization was also carried for the energy step size used in stored response functions. As demonstrated, the use of 0.1-MeV and 0.5-MeV increments between stored response functions produced similar fits that closely matched a given PuBe response. The 1-MeV increments were too large, resulting in a deviation from the measured response which was more significant than that of other increments. Further comparison of the coefficients produced by each increment indicated that the 1-MeV increment was the least suitable increment. Identification of the PuBe spectra based on this increment was extremely difficult. The use of the 0.1-MeV increment was also equally unsuitable. The 0.5-MeV increment between response functions was found to be the most suitable as it provided the best combination of a reasonable fit for the provided source response and the most easily identifiable representation of the source's expected energy spectrum.

6.2 Future Work

While the spectral unfolding was developed, there is still more work to be done. Ideally the goal will be to integrate this technique into the onboard electronics of a handheld detector system and optimize the step size used to reconstruct the neutron spectra. Additional development of a portable system which incorporates this technique into its programming is also possible. During this phase, there is also the potential to provide a display for the user which reports not just the unfolded spectra of the source or in question, but also the “certainty” of the report based on the figure of merit of pulse shape discrimination.

REFERENCES

[1] Estevan, M.T., “Consequences of the Algerciras Accident, and the Spanish System for the Radiological Surveillance and Control of Scrap and the Products of Its Processing,” *Security of Radioactive Sources*, vol. 34 pp. 357-362, 2003.

[2] Facure, A., Umisedo, N.K., Okuno, E., Yoshimura, E.M., Gomes, P.R.S., Anjos, R.M., “Remains of 137Cs Contamination in the City of Goiânia, Brazil,” *Radiation Protection Dosimetry*, vol. 95 pp. 165-171, 2001.

[3] Anjos, R.M., Umisedo, N.K., Facure, A., Yoshimura, E.M., Gomes, P.R.S., Okuno, E., “Goiânia: 12 Years after the 137Cs Radiological Accident,” *Radiation Protection Dosimetry*, vol. 101 pp. 201-204, 2002.

[4] Patlovich, S., Emery,R.J., Whitehead, L.W., “Characterization and geographic location of sources of radioactivity lost downhole in the course of oil and gas exploration and production activities in Texas, 1956 to 2001,” *Health Physics*. vol. 89 pp. S69-S77, 2005.

[5] Brozowski, G., Tucker, A., Cardarelli, J., “Response To Lost AmBe Source In West Texas,” (April, 2013).

[6] IAEA Incident and Trafficking Database (ITDB), “IAEA Incident and Trafficking Database: Incidents of Nuclear and Other Radioactive Material Out of Regulatory Control 2014 Fact Sheet,” 2014.

[7] Kouzes, R.T, Conlin, K.E., Ely, J.H., Erikson, L.E., Kernan, W.J., Lintereur, A.T., Siciliano, E.R., Stephens, D.L., Stromswold, D.C., Van Ginhoven, R. M., Woodring, M.L., “Alternatives to ^{3}He for Neutron Detection for Homeland Security,” 42 (2010) v.

[8] Kouzes, R.T., “The ^{3}He Supply Problem,” Pnnl-18388, Pacific Northwest National Laboratory, Richland, Wa. (2009).

[9] Kouzes, R.T., Ely,J.H., Erikson,L.E., Kernan,W.J., Lintereur,A.T., Siciliano,E.R., Stephens,D.L., Stromswold,D.C., Van Ginhoven,R.M., Woodring,M.L., “Neutron Detection Alternatives to ^{3}He for National Security Applications,” *Nucl. Instrum. Meth*., vol. 623 pp. 1035-1045, 2010.

[10] Shea, D.A., Morgan, D., “The Helium-3 Shortage: Supply, Demand, and Options for Congress,” Federation of American Scientists, 2011.

[11] Flakus., F.N., “Detecting and Measuring Ionizing Radiation - A Short History,” IAEA Bull., vol. 23 pp. 31-36, 1981.

[12] Knoll, G.F., *Radiation Detection and Measurement* (4th ed.), J. Wiley, New York, 2010.

[13] Leo, W.R., *Techniques for Nuclear and Particle Physics Experiments: A How-to Approach*, Springer-Verlag, Berlin; New York, 1987.

[14] van Loef, E.V., Glodo, J., Shirwadkar, U., Zaitseva, N., Shah, K.S., “Solution Growth and Scintillation Properties of Novel Organic Neutron Detectors,” *Nucl. Instrum.*

Meth., vol. 652 pp. 424-426, 2011.

[15] Iwanowska, J., Swiderskia, L., Moszynski, M., Szczesniak, T., Sibczynski, P., Galunov, N.Z., Karavaeva, N.L., "Neutron/gamma Discrimination Properties of Composite Scintillation Detectors," *JINST*., vol. 6, 2011.

[16] Cester, D., Nebbia, G., Stevanato, L., Pino, F., Sajo-Bohus, L., Viesti. G., "A Compact Neutron–Gamma Spectrometer," *Nucl. Instrum. Meth*., vol. 719 pp. 81-84, 2013.

[17] Sulyaev, Y.S., Puryga, E.A., Khilchenko, A.D., Kvashnin, A.N., Polosatkin, A.V., Rovenskikh, A.F., Burdakov, A.V., Grishnyaev, E.V., "Multi-purpose fast neutron spectrum analyzer with real-time signal processing," *Nucl. Instrum. Meth*., vol. 720 pp. 23-25, 2013.

[18] ELJEN Technology, EJ-309 Liquid Scintillator Pulse-Shape Discrimination Properties, (September, 2010).

[19] Brooks, F.D., Klein, H., "Neutron Spectrometry—Historical Review And Present Status," *Nucl. Instrum. Meth*., vol. 476 pp. 1-11, 2002.

[20] Kaschuck, Y.A., Esposito, B., Trykov, L.A., Semenov, V.P., "Fast neutron spectrometry with organic scintillators applied to magnetic fusion experiments", *Nucl. Instrum. Meth*., vol. 476 pp. 511-515, 2002.

[21] Reginatto, M., "Overview Of Spectral Unfolding Techniques And Uncertainty Estimation," *Radiat.Measur*., vol. 45 pp. 1323-1329, 2010.

[22] Poyarkov, V.A., Sadovnikova, T.S., Chikai, I., Shudar, S., "A Comparison Of Methods Of Neutron-Spectrum Unfolding," *Soviet Atomic Energy*, vol. 67 pp. 708-710, 1989.

[23] Anykeyev, V.B., Spiridonov, A.A., Zhigunov, V.P., "Comparative Investigation of Unfolding Methods," *Nucl. Instrum. Meth*., vol. 303 pp. 350-369, 1991.

[24] Matzke, M., "Unfolding Procedures," *Radiation Protection Dosimetry*, vol. 107 pp. 155-174, 2003.

[25] Lin, Y., "Wavelet-Fractional Fourier Transforms," *Chinese Physics B*, vol. 17 pp. 170, 2008.

[26] Strang, G., "Wavelet Transforms Versus Fourier-Transforms," *Bull. Amer. Math. Soc.*, vol. 28 pp. 288-305, 1993.

[27] Daubechies, I., "Ten Lectures On Wavelets," *Society for Industrial and Applied Mathematics*, Philadelphia, Pa., 1992.

[28] Mix, D.F., Olejniczak, K.J., *Elements of Wavelets for Engineers and Scientists*, Wiley-Interscience, Hoboken, NJ, 2003.

[29] Rioul, O., Duhamel, P., "Fast algorithms for discrete and continuous wavelet transforms, Information Theory," *IEEE Transactions*, vol. 38 pp. 569-586, 1992.

[30] Zheng, Y., Wu, H., Cao, L., "Application Of The Wavelet Expansion Method In

Spatial-Angular Discretization Of The Neutron Transport Equation," *Ann. Nucl. Energy*, vol. 43 pp. 31-38, 2012.

[31] Nasif, H., Omori, R., Suzuki, A., "Improved Solution of the Neutron Diffusion Equation Using Wavelet Theory," *J Nucl Sci Technol*., vol. 36 pp. 839, 1999.

[32] Nasif, H., Omori, R., Suzuki, A., Naguib, M., Nagy, M.. "Wavelet-Based Algorithms for Solving Neutron Diffusion Equations," *J Nucl Sci Technol*., vol. 38 pp. 161, 2001.

[33] Shippen, D.I., Joyce, M.J., Aspinall, M.D., "A Wavelet Packet Transform Inspired Method of Neutron-Gamma Discrimination," *IEEE Trans.Nucl.Sci*., vol. 57 p. 2617-2624, 2010.

[34] Garcia-Belmonte, G., Hernandez, R., Fernandez-Marron, J.L., Perez, J.M., "Nuclear Pulse Processing Using The Discrete Wavelet Transform," *Applied Signal Processing*, vol. 3 pp. 192-198, 1996.

[35] Garcia-Belmonte, G., Perez, J.M., Fernandez-Marron, J.L., Bisquert, J., "Digital Implementation Of Filters For Nuclear Applications Using The Discrete Wavelet Transform," *Nucl. Instrum. Meth*., vol. 380 pp. 376-380, 1996.

[36] Rekik, S., Guerchi, D., Selouani, S., Hamam, H., "Speech Steganography Using Wavelet and Fourier Transforms," *EURASIP Journal on Audio, Speech, and Music Processing*, vol. 2012 pp. 1-14, 2012.

[37] Johnson, R.M., A User's Manual for COOLC and FORIST, PNE-75-107 (1975).

[38] Reginatto, M., Goldhagen, P., "A Computer Code for Maximum Entropy Deconvolution of Multisphere Neutron Spectrometer Data," *Healthy Phys.*, vol. 77 p. 579-583, 1999.

[39] Physikalisch-Technische Bundesanstalt (PTB), Braunschweig, Germany. UMG 3.3 – Unfolding With Maxed and Gravel, RSICC Code Package, PSR-529. (March, 2004).

[40] WH Press, *Numerical recipes in FORTRAN: The Art of Scientific Computing*, Cambridge University Press Cambridge, Cambridge, 1992.

[41] Dehimi, F.Z., Seghour, A., El Hak Abaidia, S., "Unfolding of Neutron Energy Spectra With Fisher Regularisation," *IEEE Transactions on Nuclear Science*, vol. 57 pp. 768-774, 2010.

[42] Ortiz-Rodríguez, J.M., Alfaro, A.R., Haro, A.R., Solís Sánches, L.O., Miranda, M.C., Cervantes Viramontes, J.M., Vega-Carrillo, H.R., "Evaluating The Performance Of Two Neutron Spectrum Unfolding Codes Based On Iterative Procedures And Artificial Neural Networks," *AIP Conference Proceedings*, vol. 1544 pp. 114-121, 2013.

[43] Sundén, E.A., Sjöstrand, H., Weiszflog, M., Gorini, G., Tardocchi, M., JET EFDA contributors, S. Conroy, S., Ericsson, G., Johnson, M.G., Giacomelli, L., Hellesen, C., Hjalmarsson, A., Källne, J., Ronchi, E., "Evaluation Of Spectral Unfolding Techniques For Neutron Spectroscopy," *AIP Conference Proceedings*, vol. 988 pp. 315, 2008.

[44] Zech, G., "Iterative Unfolding With The Richardson–Lucy Algorithm," *Nucl.*

Instrum. Meth., vol. 716 pp. 1-9, 2013.

[45] Sanna, R., O'Brien, K., “Monte-Carlo Unfolding Of Neutron Spectra,” *Nucl. Instrum. Meth.*, vol. 91 pp. 573-576, 1971.

[46] Freeman, D.W., Edwards, D.R., Bolon, A.E., “Genetic Algorithms – A New Technique For Solving The Neutron Spectrum Unfolding Problem,” *Nucl. Instrum. Meth.*, vol. 425 pp. 549-576, 1999.

[47] Suman. V., Sarkar, P.K., “Neutron Spectrum Unfolding Using Genetic Algorithm In A Monte Carlo Simulation,” *Nucl. Instrum. Meth.*, vol. 737 pp. 76-86, 2014.

[48] Mukherjee, B., “A High-Resolution Neutron Spectra Unfolding Method Using The Genetic Algorithm Technique,” *Nucl. Instrum. Meth.*, vol. 476 pp. 247-251, 2002.

[49] Santos, J.A.L., Silva, E.R., Ferreira, T.A.E., Vilela, E.C., “Unfolding Neutron Spectra Obtained From BS–TLD System Using Genetic Algorithm,” *Applied Radiation and Isotopes*, vol. 71 Supplement, pp. 81-86, 2012.

[50] Shore, J., Johnson, R., “Axiomatic Derivation Of The Principle Of Maximum Entropy And The Principle Of Minimum Cross-Entropy,” *IEEE Transactions on Information Theory*, vol. 26 pp. 26-37, 1980.

[51] Los Alamos National Laboratory, A General Monte Carlo N-Particle Transport Code, LAUR-03-1987, 5 (April, 2003).

[52] Pozzi, S.A., Bourne, M.M., Clarke, S.D., “Pulse Shape Discrimination In The Plastic Scintillator EJ-299-33,” *Nucl. Instrum. Meth.*, vol. 723 pp. 19-23, 2013.

[53] ELJEN Technology, EJ-299-33A PSD Plastic Scintillator, (April, 2014).

[54] The MathWorks Inc., MATLAB R2012b Student Edition, 8.0.0.783 (2012).

[55] Misiti, M., Misiti, Y., Oppenheim, G., Poggi,J.M., *MATLAB: Wavelet Toolbox User's Guide*, The MathWorks, Inc., Natick, Massachusetts, 2014.

[56] Chapra, S.C., *Applied Numerical Methods With MATLAB For Engineers And Scientists* (3rd ed.), McGraw-Hill Higher Education, Boston, 2012.

[57] Smith, A.B., Fields, P.R., Roberts, J.H., “Spontaneous Fission Neutron Spectrum of Cf^{252},” *Phys. Rev.* vol. 108 pp. 411-413, 1957

[58] Xu, Y., Flaska, M., Pozzi, S., Protopopescu, V., Downar, T., “A Sequential Least-Squares Algorithm for Neutron Spectrum Unfoling from Pulse-Height Distributions Measured with Liquid Scintillators,” (2007).

[59] Lawrence, C.C., Enqvist, A., Flaska, M., Pozzi, S.A., Becchetti, F.D., “Comparison of Spectrum-Unfolding Performance of (EJ315) and (EJ309) liquid scintillators on measured ^{252}Cf Pulse Height Spectra,” *Nucl. Instrum. Meth.*, vol. 729 pp. 924-929, 2013.

[60] Zak, T., Clarke, S.D., Bourne, M.M., Pozzi, S.A., Xu, Y., Downar, T.J., Peerani, P., “Neutron Spectroscopy of Plutonium Oxide Using Matrix Unfolding Approach,” *Nucl. Instrum. Meth.*, vol. 622 pp. 191-195, 2010.

[61] Pozzi, S.A., Mullens, J.A., Mihalczo, J.T., “Analysis Of Neutron And Photon

Detection Position For The Calibration Of Plastic (BC-420) And Liquid (BC-501) Scintillators," *Nucl. Instrum. Meth*., vol. 524 pp. 92-101, 2004.

[62] Pozzi, S.A., Mullens, J.A., Mihalczo, J.T., "Calibration of Small Plastic Scintillators for Imaging Applications," ORNL/TM-2004/298 (December 2004).

[63] Liskien, H., Paulsen, A., *Neutron production cross sections and energies for the reactions T(p,n)3He, D(d,n)3He, and T(d,n)4He, Atomic Data and Nuclear Data Tables*, 1973.

[64] Harvey, Z.R. Neutron Flux And Energy Characterization of a Plutonium-Beryllium Isotopic Neutron Source By Monte Carlo Simulation With Verification By Neutron Activation Analysis. (2010).

VITA

Graduate College
University of Nevada, Las Vegas

Jessica Hartman

Degree:

Bachelor of Science, Mechanical Engineering, 2012
University of Nevada, Las Vegas

Publications:

Hartman, J., Richardson, N., Barzilov, A., Dual Neutron Photon Radiography Using a Single Imaging Detector Array, ASNT 23rd Research Symposium. (2014).

Hartman, J., Barzilov, A., Evaluation of Performance of Neutron Spectrum Unfolding Technique Based on Wavelets, ANS 2014 Student Conference (2014).

Hartman, J., Barzilov, A., Computational Feasibility Study of Dual Photon/Neutron Imaging Technique, ASNT 23rd Research Symposium (2014).

Hartman, J., Barzilov, A., Application of Wavelet Unfolding Technique in Neutron Spectroscopic Analysis, 23rd International Conference on the Application of Accelerators in Research and Industry, Physics Procedia. (2014).

Hartman, J., Barzilov, A., Computational Study of Integrated Neutron/Photon Imaging for Illicit Material Detection, Physics Procedia. (2014).

Barzilov, A., Hartman, J., Richardson, N., Measurements of Fast Neutron Flux Using an Array of EJ-299-33A Scintillator Detectors, ANS 2014 Annual Meeting Proceedings. (2014).

Thesis Title:

Neutron Spectroscopy With Scintillation Detectors Using Wavelets

Thesis Examination Committee:

Chairperson, Alexander Barzilov, Ph. D.
Committee Member, William Culbreth, Ph. D.
Committee Member, Yitung Chen, Ph. D,
Graduate Faculty Representative, Gary Cerefice, Ph.D.